JPL PUBLICATION 84-6

Aerosol Backscatter Lidar Calibration and Data Interpretation

Michael J. Kavaya
Robert T. Menzies

March 1, 1984

NASA
National Aeronautics and
Space Administration

Jet Propulsion Laboratory
California Institute of Technology
Pasadena, California

JPL PUBLICATION 84-6

Aerosol Backscatter Lidar Calibration and Data Interpretation

Michael J. Kavaya
Robert T. Menzies

March 1, 1984

National Aeronautics and
Space Administration

Jet Propulsion Laboratory
California Institute of Technology
Pasadena, California

The research described in this publication was carried out by the Jet Propulsion Laboratory, California Institute of Technology, under contract with the National Aeronautics and Space Administration.

ABSTRACT

This report presents a treatment of the various factors involved in lidar data acquisition and analysis. This treatment highlights sources of fundamental, systematic, modeling, and calibration errors that may affect the accurate interpretation and calibration of lidar aerosol backscatter data. The discussion primarily pertains to ground-based, pulsed-CO_2 lidars that probe the troposphere and are calibrated using large, hard calibration targets. However, a large part of the analysis is relevant to other types of lidar systems such as lidars operating at other wavelengths; continuous-wave (cw) lidars; lidars operating in other regions of the atmosphere; lidars measuring nonaerosol elastic or inelastic backscatter; airborne or Earth-orbiting lidar platforms; and lidars employing combinations of the above characteristics.

CONTENTS

Figures

SECTION 1

INTRODUCTION

Measurements of the aerosol volume backscatter coefficients at CO_2 laser wavelengths not only provide an improved understanding of large aerosol particles in the atmosphere but also are very important for assessing the requirements of Earth-orbiting CO_2 lidars for measurements of atmospheric winds and other parameters. In particular, remote measurements of winds on a global scale are essential for a better understanding of processes taking place within the Earth's troposphere. In order for us to understand climatic and weather-related processes, measurements must be made of the wind vectors as a function of latitude, longitude, altitude, time, and weather conditions. Studies indicate such tropospheric-wind field data would greatly enhance the accuracy of the National Weather Service's 12 hour-5 day forecasts. There is general agreement that the infrared coherent Doppler lidar technique, of all the candidate passive and active atmospheric measurement techniques that may be implemented from an orbiting platform, offers the greatest potential for global tropospheric-wind measurements. Since the return signal from a given range is directly proportional to the aerosol backscatter coefficient in that region, uncertainties in the knowledge of the backscatter coefficient imply corresponding uncertainties in the required laser-transmitter pulse energy and receiver-telescope diameter. Therefore, measurements of the aerosol backscatter coefficient at CO_2 laser wavelengths as a function of latitude, longitude, altitude, time, and weather conditions are critical.

A number of CO_2 lidar systems are in use or are proposed that will contribute to enlarging the aerosol backscatter coefficient data base. These include fixed-location, ground-mobile, and airborne systems; and both

pulsed and continuous-wave (cw) focused. At JPL, we have been operating a fixed, pulsed-CO_2 lidar over the past two years in order to measure the tropospheric aerosol backscatter coefficient in the 9 to 11 μm region.

Since quantitative values of the backscatter coefficient are desired, a technique for accurately calibrating the backscatter data has been developed that uses a large, hard surface as a lidar calibration target. The use of the total backscatter to Rayleigh backscatter ratio technique, which is often used in the visible wavelength region to calibrate lidar responsiveness and consequently to obtain aerosol backscatter coefficients (Russell, Swissler, and McCormick, 1979), does not apply at mid-infrared wavelengths. The assumption that backscatter and extinction are related through a functional relationship, such as a power-law relationship (Klett, 1981, 1983), also does not apply. In the mid-infrared the Rayleigh backscatter is extremely low, and the atmospheric extinction is usually dominated by molecular species rather than by the aerosol itself. Thus a hard-target calibration technique is used.

The measurement of a single vertical profile of aerosol backscatter requires many individual shots of the lidar system in close temporal proximity both in the vertical direction through the atmosphere and at the calibration target. Each lidar pulse results in a digitized record of transmitted power vs. time and received (backscattered) power vs. time. These data records must be processed appropriately and then combined with the pertinent characteristics of the lidar system and parameters of the atmosphere and calibration target in order to calculate the desired aerosol-backscatter range profile correctly.

The purpose of this report is to discuss many aspects of this complicated and multifaceted calibration and data interpretation process. It is hoped that this discussion will contribute to an accurate and consistent

calibration of lidar data. Although the authors' primary experience is with a stationary, pulsed-CO_2 lidar system, much of the discussion will be useful in calibrating backscatter data from ground-mobile and airborne lidar systems, from lidar systems operating at other wavelengths, and from cw-focused lidar systems.

SECTION 2

LIDAR BACKSCATTER SIGNALS

2.1 ATMOSPHERIC AEROSOL BACKSCATTER SIGNAL

Consider a pulsed infrared lidar system directed into the atmosphere. Assume collinear or near-collinear (side-by-side) geometry for the transmitter and receiver telescopes and assume that both telescopes subtend very small solid angles at the ranges of interest. Let the transmitted pulse start at time $t = 0$ and end at time $t = \tau_p$ with a power profile of $P_{tb}(t)$ [W], as shown in Figure 1a. The received power [W] due to aerosol backscatter is then given by

$$P_b(t) = \int_{c(t-\tau_p)/2}^{ct/2} P_{tb}(t - \frac{2R}{c})\, \beta(R)\, \frac{A}{R^2}\, \eta\, O(R)\, \exp\{-2 \int_0^R \alpha_b(R')dR'\}dR \qquad (1)$$

where A is the effective receiver area, R is the line-of-sight range from the telescopes, $AR^{-2} = \omega_r(R)$ [sr] is the solid angle subtended by the receiver, η is the system's optical efficiency, $O(R)$ is the range-dependent telescope overlap function defined as the fraction of the transmitted pulse energy that is within the receiver's field-of-view (FOV), $\alpha_b(R)$ [m^{-1}] is the total extinction coefficient of the atmosphere along the optical path, $\beta(R)$ [$m^2\ m^{-3}\ sr^{-1} = m^{-1}\ sr^{-1}$] is the aerosol volume backscatter coefficient defined as the fraction of incident energy scattered in the backward direction per unit solid angle per unit atmospheric length, and where the integration over R indicates that the received power at time t is due to contributions from a slab of atmosphere of thickness $c\tau_p/2$ centered at $R_b = c(t/2-\tau_p/4)$. (A list of symbols used in this and following equations, along with their definitions, can be found in Appendix A.) Other sources of received power at time t, such

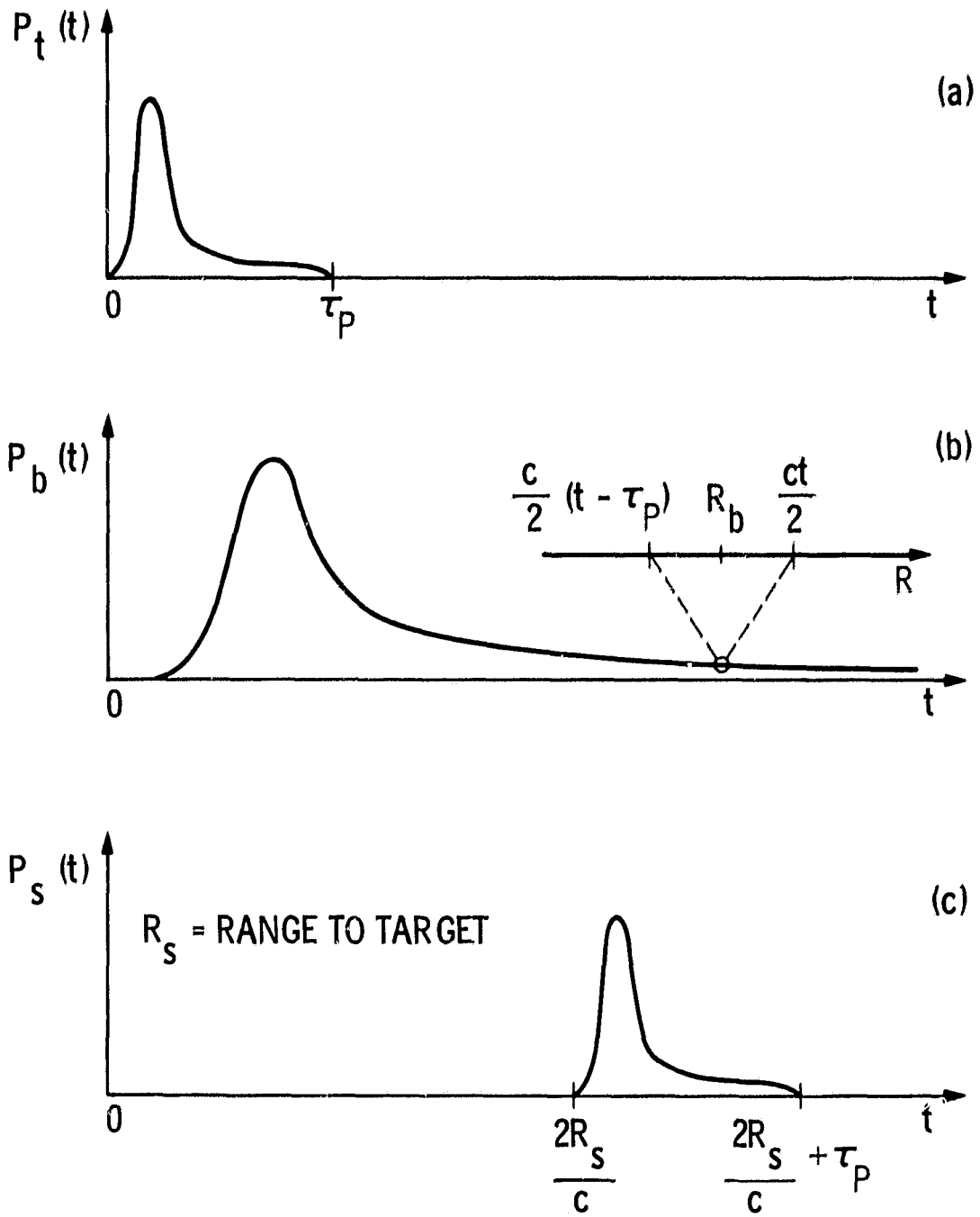

Figure 1. Pulsed lidar temporal profile examples for (a) the transmitted laser pulse power, (b) the backscattered power from the atmospheric aerosol, and (c) the backscattered power from a hard target.

as multiple scattering, Rayleigh scattering, resonant fluorescence, fluorescence, and Raman scattering, are neglected. Monochromatic transmitted radiation is assumed, and thus the wavelength dependence of $\beta(R)$, n, $O(R)$, and $\alpha_b(R)$ is understood. If the receiver employs heterodyne detection, then $\beta(R)$ in Equation (1) refers only to the backscattered radiation with polarization parallel to the polarization of the local oscillator. Figure 1b depicts the aerosol backscatter signal.

The desired quantity is the backscatter coefficient range profile, $\beta(R)$. From Equation (1) we see that the maximum spatial frequency of $\beta(R)$ along the optical path that can be determined is on the order of $2/(c\tau_p)$. This causes a bias against the measurement of low values of $\beta(R)$ that might occur over spatial distances smaller than $c\tau_p/2$. The smoothing function that operates on $\beta(R)$ is not rectangular but is shaped by the range-dependent terms in Equation (1). If we now assume that both $\beta(R)$ and $O(R)$ are slowly varying compared to the spatial distance $c\tau_p/2$, then Equation (1) becomes

$$P_b(t) = \beta(R_b)\, A\, n\, O(R_b) \int_{c(t-\tau_p)/2}^{ct/2} P_{tb}(t-\tfrac{2R}{c})\, R^{-2} \exp\{-2\int_0^R \alpha_b(R')dR'\}dR \qquad (2)$$

At this point we are able to solve for $\beta(R)$ if all of the terms in Equation (2) are known accurately. Equation (2) is still exact under the stated assumptions. A further simplification of Equation (2), which is commonly used, is to assume that the entire integrand except $P_{tb}(t)$ is constant over the integration range, yielding

$$P_b(t) = \beta(R_b)\frac{A}{R_b^2}\eta\, O(R_b)\exp\{-2\int_0^{R_b}\alpha_b(R')dR'\}\int_{c(t-\tau_p)/2}^{ct/2} P_{tb}(t-\frac{2R}{c})dR$$

$$= \beta(R_b)\frac{A}{R_b^2}\eta\, O(R_b)\exp\{-2\int_0^{R_b}\alpha_b(R')dR'\}\frac{c}{2}\int_0^{\tau_p} P_{tb}(t)\,dt \qquad (3)$$

This simplification can lead to errors in the calculated value of $\beta(R)$ and will be discussed later. The remaining integral in Equation (3) is simply the pulse energy [J]:

$$E_{tb} = \int_0^{\tau_p} P_{tb}(t)\,dt \qquad (4)$$

Often the pulse power profile of Figure 1a is assumed to be rectangular with power P_0. In this case $E_{tb} = P_0\tau_p$.

2.2 HARD-TARGET BACKSCATTER SIGNAL

Consider the same pulsed lidar system directed at a calibration target that is at a range R_s from the telescopes. Let the target be larger than both the laser spot size at R_s and the receiver field-of-view at R_s, and let the polar angle between the optical axis and the average surface normal of the target be θ. If the pulse in Figure 1a ($P_{ts}(t)$ in this hard-target case) is transmitted, the received power [W] is given by

$$P_s(t) = P_{ts}\left(t-\frac{2R_s}{c}\right)\rho^*\frac{A}{R_s^2}\eta\, O(R_s)\exp\{-2\int_0^{R_s}\alpha_s(R')dR'\} \qquad (5)$$

where $\alpha_s(R)$ [m^{-1}] is again total extinction and is most likely different from $\alpha_b(R)$ due to the different atmospheric paths employed, ρ^* [sr^{-1}]

is the target parameter defined as the reflected power per steradian toward the receiver divided by the incident power (Kavaya et al., 1983), $2R_s/c$ is the round-trip transit time of light, and aerosol backscatter is added to the earlier list of neglected sources of received power at time t. Note that the received-power profile is identical to the transmitted-power profile, but is delayed by $2R_s/c$ seconds. This is depicted in Figure 1c. We will neglect the spread in the distance to the target caused by the target angle θ and the finite beam diameter.

2.3 SINGLE-PULSE HARD-TARGET CALIBRATION OF $\beta(R)$

Let us assume a very simple case in which one lidar pulse is fired at the atmosphere and one pulse is fired at the calibration target. Although Equation (2) is more exact than Equation (3), seldom are all the terms in Equation (2) known accurately. Furthermore, often a signal proportional to transmitted pulse energy E_{tb} is recorded for normalization and, therefore, an expression for received power that is proportional to E_{tb}, such as Equation (3), is desired. Comparing Equations (3) and (5), we see that the integral of the target return profile given by Equation (5) must be calculated. This integral I_s [J] is given by

$$I_s = \int_{\frac{2R_s}{c}}^{\frac{2R_s}{c}+\tau_p} P_s(t)dt = \rho^* \frac{A}{R_s^2} \eta\, O(R_s) \exp\{-2\int_0^{R_s} \alpha_s(R')dR'\}\, E_{ts} \qquad (6)$$

(We are assuming at this point that a sufficiently fast transient digitizer is used to record $P_s(t)$ so that an accurate integral is possible. Alternatively,

an integrating analog-to-digital (A/D) converter with a gate width that captures the return pulse may be used if the signal voltage is proportional to $P_s(t)$.) Combining Equations (3) and (6) we see that

$$\beta(R_b) = \frac{P_b(t)}{E_{tb}} \frac{E_{ts}}{I_s} \rho^* \frac{2}{c} \frac{R_b^2}{R_s^2} \frac{O(R_s)}{O(R_b)} \frac{\exp\{-2 \int_0^{R_s} \alpha_s(R')dR'\}}{\exp\{-2 \int_0^{R_b} \alpha_b(R')dR'\}} \tag{7}$$

where we let the atmospheric and target pulses have energies E_{tb} and E_{ts}, respectively. Even in this simple example in which fluctuations of the returned signal intensity due to speckle and atmospheric turbulence are ignored, and in which an adequate signal-to-noise ratio is assumed from one lidar pulse, it is clear that the lidar pulse energies; the target parameter, ρ^*; the telescope overlap function, $O(R)$; and the extinction profiles, $\alpha_s(R)$ and $\alpha_b(R)$, must be well-known. In addition, the assumptions and simplifications leading to Equations (3) and (6) cannot be ignored.

SECTION 3

DATA ACQUISITION ERRORS

The discussion leading to Equation (7) assumed that the transmitted-pulse profiles, $P_{tb}(t)$ and $P_{ts}(t)$; the aerosol backscatter signal, $P_b(t)$; and the target backscatter signal, $P_s(t)$, were all known in their fundamental units of watts. In reality, detectors are used to convert the optical fields into a voltage (or current), followed by preamplifiers, amplifiers, filters, etc. Finally, this voltage is recorded for later processing. We may lump all of the characteristics of this chain of components (or receiver) into a single function that operates on the optical signal power:

$$V(t) = F_1\{P(t)\} \tag{8}$$

where $V(t)$ [V] is the recorded signal available for processing and is not necessarily a linear function of $P(t)$. We may factor the function F_1 into various typical subfunctions, such as the gain G of the receiver and the largest time constant τ of the receiver, which represents the slowest element in the chain. Thus Equation (8) can be written

$$V(t) = G \times F_2\{P(t)\} * \left[\frac{1}{\tau} \exp(-t/\tau) \times H(t)\right] \tag{9}$$

where the symbol * stands for the convolution operation and $H(t)$ is the Heaviside unit step function. (Convolution in the time domain corresponds to multiplication in the frequency domain. In Equation (9) the spectrum of $G \times F_2\{P(t)\}$ is multiplied by $[1 + (2\pi f\tau)^2]^{-1/2}$.) In general, the recorded voltages from the transmitted pulse, the aerosol backscatter, and the target backscatter are given by

$$V_t(t) = G_t \times F_t\{P_t(t)\} * \left[\frac{1}{\tau_t} \exp(-t/\tau_t) \times H(t)\right] \quad (10a)$$

$$V_b(t) = G_b \times F_b\{P_b(t)\} * \left[\frac{1}{\tau_b} \exp(-t/\tau_b) \times H(t)\right] \quad (10b)$$

$$V_s(t) = G_s \times F_s\{P_s(t)\} * \left[\frac{1}{\tau_s} \exp(-t/\tau_s) \times H(t)\right] \quad (10c)$$

We are assuming that the slowest element of the receiver is much slower than the next slowest element and that this element can be approximated by a simple RC low-pass filter (τ = RC), and we also assume that any DC offsets that are added to V(t) can be determined and removed. The impulse responses of the low-pass filters, the exponential terms in brackets, are normalized to have an area of 1. Thus the area under V(t) is equal to the area under G × F{P(t)} (Bracewell, 1978). The centroid of V(t) occurs τ s after the centroid of G × F{P(t)}. The spread of V(t) about its centroid (similar to variance) is τ^2 s^2 greater than the spread of G × F{P(t)}. Frequency components of G × F{P(t)} much less than $1/\tau$ are not attenuated, while frequencies much greater than $1/\tau$ fall as 1/f. If τ approaches 0 (as with very fast receiver components), then the RC-filter impulse response approaches $\delta(t)$ and the convolutions in Equation (10) can be neglected.

Strictly, the first four terms in the right side of Equation (7) must be replaced by appropriate expressions using Equation (10). Equation (10a) must be applied twice to solve for $P_{tb}(t)$ and $P_{ts}(t)$, which are then substituted into Equation (4) to obtain E_{tb} and E_{ts}. Equation (10b) must be solved for $P_b(t)$ and Equation (10c) must be solved for $P_s(t)$, which is then substituted into Equation (6) to obtain I_s. Fortunately, several simplifications of this procedure are possible. It was stated earlier that the

convolution operator in Equation (10) does not affect the area under V(t), but does spread V(t) in time with respect to F{P(t)}. Since Equation (4) is used twice with Equation (10a) to take time integrals, the convolution in Equation (10a) may be neglected, provided that the upper integration limit in Equation (4) is extended to include all of $V_t(t)$ and provided that the function F_t is linear. We will make these assumptions and thus Equation (10a) reduces to

$$V_{tb}(t) = G_t P_{tb}(t) \tag{11a}$$

$$V_{ts}(t) = G_t P_{ts}(t) \tag{11b}$$

The assumption that the function F_t is linear is reasonable since linear detectors are usually used to monitor pulse power. Note in Equation (11) that it is also assumed that the gain, G_t, is constant. Actually, G_t is a function of the wavelength, λ, and may also depend on P_t and time. If only a small portion of the pulse cross section is imaged onto the pulse-power detector, then pulse-to-pulse variations in the pulse spatial profile may cause variations in the fraction of pulse power incident on the detector. In effect, a pulse-to-pulse (or time) variation in G_t results.

It is not quite as reasonable to eliminate the convolutions in Equations (10b) and (10c), since often a lidar receiver is not linear in received power. Two common nonlinear examples of the functions F_b and F_s are $\sqrt{P}$ or ℓnP. The fact that $P_b(t)$ probably does not have frequency components of interest greater than $1/\tau_b$ allows the convolution in Equation (10b) to be eliminated. Even though Equation (6) is used to integrate $P_s(t)$, the convolution in Equation (10c) may not be ignored unless F_s is linear or

τ_s is very small. Nevertheless, we will neglect the convolution in Equation (10c), thus introducing a source of error in calculating $\beta(R)$. It is usually the case that $F_b = F_s = F_r$, where the subscript r refers to the lidar receiver. Often the gain of the receiver is adjusted between firing at the atmosphere and firing at the calibration target due to the much larger signal from the target. In addition, the gains G_b and G_s may depend on the received powers P_b and P_s and on the bandwidth of the received power. Obviously, the bandwidth of $P_s(t)$ will be much greater than the bandwidth of $P_b(t)$. These effects on the receiver gain can introduce errors if not accounted for. We will ignore these effects in what follows and simplify Equations (10b) and (10c) to

$$V_b(t) = G_b \times F_r\{P_b(t)\} \tag{12a}$$

$$V_s(t) = G_s \times F_r\{P_s(t)\} \tag{12b}$$

Combining Equations (4), (6), (11), and (12), we find that the first four terms in the right side of Equation (7) become

$$\frac{P_b(t)}{E_{tb}} \times \frac{E_{ts}}{I_s} = \frac{F_r^{-1}\{V_b(t)/G_b\}}{\int_0^{\tau_p} V_{tb}(t)dt} \times \frac{\int_0^{\tau_p} V_{ts}(t)dt}{\int_{\frac{2R_s}{c}}^{\frac{2R_s}{c}+\tau_p} F_r^{-1}\{V_s(t)/G_s\}dt} \tag{13}$$

where the factors G_t in Equation (11) have canceled and $F_r^{-1}\{x\}$ represents the inverse operation of $F_r\{x\}$. For example, the inverse of $\sqrt{x}$ and ℓnx would be x^2 and e^x, respectively. At this point we observe a major difference between the linear, square-root, and logarithmic lidar receiver functions F_r. As stated earlier, the gains G_b and G_s are often purposely made different due to the larger return from calibration targets than from the atmospheric aerosol. In practice, it is much easier to know the ratio of these gains G_s/G_b than it is to know both their values independently. From Equation (13) it is clear that the ratio G_s/G_b is sufficient to calculate $\beta(R)$ for linear and square-root lidar receivers, where $F_r^{-1}\{x\} = x$ and x^2, respectively. However, for a logarithmic receiver, $F_r^{-1}\{x\} = e^x$, and the actual values of G_b and G_s are required to solve for $\beta(R)$. This suggests that logarithmic receivers are not appropriate if lidar aerosol backscatter data are to be calibrated using hard targets.

It has been assumed in this section that a sufficiently fast transient digitizer is used to record $V_{tb}(t)$, $V_{ts}(t)$, $V_b(t)$, and $V_s(t)$. Another type of A/D converter that is often used is an integrating A/D converter. These devices usually have a variable gate width and integrate the voltage waveform during the gate period. It is clear from Equations (4) and (11) that an integrating A/D converter is acceptable to record the pulse energy signals, provided that the detector is linear in power. From Equations (12) and (13), however, it is apparent that the use of an integrating A/D converter would be appropriate for $V_b(t)$ and $V_s(t)$ only if the function F_r is linear in power. For nonlinear lidar receivers, errors would be caused when an integrating A/D was used, especially with the higher-frequency calibration-target return signal $V_s(t)$.

SECTION 4

DATA PROCESSING ERRORS

4.1 SIGNAL-AVERAGING

We have derived an expression for $\beta(R)$, given by Equations (7) and (13), for the case of a single lidar pulse directed into the atmosphere and a single lidar pulse directed at a calibration target. The energy of each pulse was used to normalize the return signals. It was assumed that the signal-to-noise ratios were adequate and that both speckle and atmospheric turbulence effects were not present. In reality, the received-power profiles from both the calibration target and the atmospheric aerosol will fluctuate from pulse to pulse due to speckle and atmospheric turbulence. These sources of signal fluctuation and the desire to improve low signal-to-noise ratios usually make it mandatory to signal-average the results of many lidar pulses.

We now consider a measurement consisting of N_b pulses fired into the atmosphere and N_s pulses fired at the calibration target. We assume all the terms in Equation (7) remain constant during the measurement except the four terms given in Equation (13). (Of course, the extinction profiles $\alpha_b(R)$ and $\alpha_s(R)$, as well as $\beta(R)$ itself, may change during the measurement time, due to temporal changes of the atmosphere or due to spatial movement of the lidar system, thus introducing a source of error. This again causes a bias against low β values that may exist for narrow spatial or temporal ranges.) Since normalization by the pulse energy will be discussed in a later section, it is assumed here that all pulses are identical, allowing cancellation of the two pulse-energy integrals in Equation (13). Under these assumptions, Equation (13) becomes

$$\frac{\langle P_b(t)\rangle}{\langle I_s\rangle} = \frac{\frac{1}{N_b}\sum_{i=1}^{N_b} F_r^{-1}\{V_b^i(t)/G_b\}}{\frac{1}{N_s}\sum_{j=1}^{N_s}\int_{\frac{2R_s}{c}}^{\frac{2R_s}{c}+\tau_p} F_r^{-1}\{V_s^j(t)/G_s\}\,dt} \tag{14}$$

where $\langle\ \rangle$ indicates an ensemble-average and the superscripts i and j on $V_b(t)$ and $V_s(t)$ represent the pulse-to-pulse variation in the recorded waveforms. Often, however, Equation (14) is not used to process signal-averaged lidar data. Instead, the recorded voltage waveforms $V_b^i(t)$ and $V_s^j(t)$ are averaged and only afterward is the inverse operator F_r^{-1} applied. This often used but incorrect expression is

$$\frac{\langle P_b(t)\rangle}{\langle I_s\rangle} \neq \frac{F_r^{-1}\left\{\frac{1}{N_b G_b}\sum_{i=1}^{N_b} V_b^i(t)\right\}}{\int_{\frac{2R_s}{c}}^{\frac{2R_s}{c}+\tau_p} F_r^{-1}\left\{\frac{1}{N_s G_s}\sum_{j=1}^{N_s} V_s^j(t)\right\}\,dt} \tag{15}$$

If F_r is a linear function, then Equation (15) is identical to Equation (14). It is interesting to calculate the error caused by using Equation (15) under typical lidar aerosol and target backscatter conditions, when F_r is a nonlinear function such as $\sqrt{P}$ or ℓnP.

Let X_i be an independent random variable with a probability density function p(x) and mean value $\langle x\rangle$. Let $Y = (1/N)\,[X_1 + X_2 + \ldots + X_N]$ have probability density p(y). By the central limit theorem, for large N,

p(y) will be a Gaussian density function with the mean value $\langle y \rangle = \langle x \rangle$. This mean value is given by

$$\langle y \rangle = \langle x \rangle = \int_{-\infty}^{\infty} x\, p(x)\, dx \tag{16}$$

and represents the correct signal-averaged result given by Equation (14). We now consider a function of x, $F_r(x)$. If we signal-average $F_r(x)$, we again obtain a Gaussian density function with a mean value equal to $\langle F_r(x) \rangle$. Following the incorrect technique of Equation (15), we now perform the inverse operation:

$$F_r^{-1}\{\langle F_r(x) \rangle\} = F_r^{-1} \left\{ \int_{-\infty}^{\infty} F_r(x)\, p(x)\, dx \right\} \tag{17}$$

The ratio of Equation (17) to Equation (16) yields the error caused by the signal-averaging technique of Equation (15), and this error obviously depends on p(x) and $F_r(x)$.

We may approximate the probability density function of the returned power in a typical lidar system due to speckle and atmospheric turbulence by the Gamma density function of order M. This function is shown inset in Figure 2 and ranges from an exponential for M = 1 to a Gaussian-like function (but with $x \geq 0$ only) for large M. The exponential (M = 1) form is predicted for fully developed speckle with no aperture-averaging. The ratio of Equation (17) to Equation (16) has been calculated for the Gamma density function and for $F_r\{x\} = \sqrt{x}$ and $\ell n x$. For $F_r\{x\} = \sqrt{x}$ the ratio is

$$\frac{\langle \sqrt{x} \rangle^2}{\langle x \rangle} = \frac{\pi}{M} \left[\frac{1 \times 3 \times 5 \times \cdots \times (2M - 1)}{(M - 1)! \times 2^M} \right]^2 \tag{18}$$

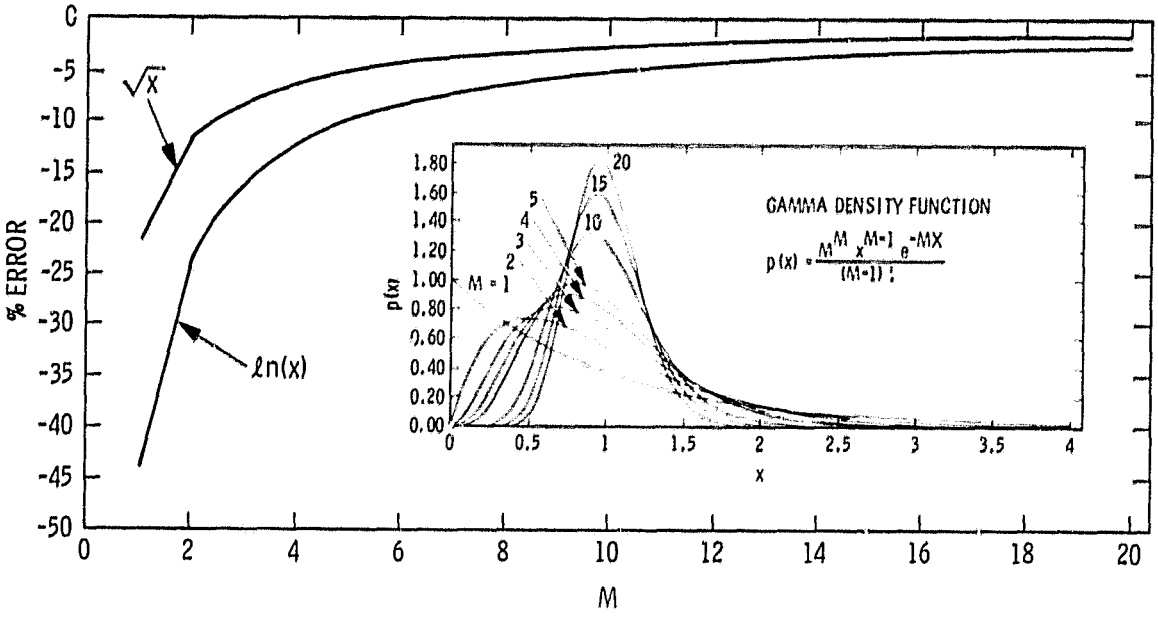

Figure 2. Calculated error in the estimated mean value of a random variable x due to averaging the functions $\sqrt{x}$ and ℓnx vs. M where the probability density function of x is the Gamma density function of order M.

which approaches 1 for large M. The percentage error is plotted in Figure 2 and reaches a maximum of -22% when M = 1. Referring to Equation (7) we see that β will be underestimated by 22%. When $F_r\{x\} = \ell nx$, the ratio is given by

$$\frac{\exp\,[\langle \ell nx \rangle]}{\langle x \rangle} = (0.561)\ M^{-1} \left[\exp \sum_{n=1}^{M-1} \frac{1}{n} \right] \tag{19}$$

which also approaches 1 for large M. As seen in Figure 2, the error in this case is greater than for $F_r\{x\} = \sqrt{x}$ and reaches a maximum of -44% for M = 1. Zrnić (1975) addressed the closely related problem of comparing $\sqrt{X}$ ("linear") and ℓnX (logarithmic) radar receivers with X ("quadratic") receivers. He treated only the M = 1 exponential power distribution (Rayleigh amplitude distribution) case and solved for both the error and standard deviation of the power estimate as a function of the number of samples, N. For large N his results are identical to our M = 1 results. He found that for large N, a "linear" receiver requires 1.09 times more samples than a "quadratic" receiver to achieve the same standard deviation, and the logarithmic receiver requires 1.64 times more samples.

It is clear that the signal-averaging technique of Equation (15) is unacceptable when the receiver function F_r is nonlinear, and the correct technique of Equation (14) should be used. Only if p(x) and $F_r\{x\}$ are well-known could the expressions of Equations (16) and (17) be used to calculate a "correction" factor for the derived values of $\beta(R)$.

4.2 PULSE-ENERGY NORMALIZATION

In the last section it was assumed that all the laser pulses had identical energies and, therefore, the terms E_{tb} and E_{ts} were equal and canceled in Equation (7). In actual practice, the transmitted pulse energy

will vary from pulse to pulse and proper normalization by pulse energy is required to avoid errors. Expanding Equation (13) to include correct signal-averaging, we obtain

$$\left\langle \frac{P_b(t)}{E_{tb}} \right\rangle \times \left\langle \frac{E_{ts}}{I_s} \right\rangle = \frac{\frac{1}{N_b} \sum_{i=1}^{N_b} \frac{F_r^{-1}\{V_b^i(t)/G_b\}}{\int_0^{\tau_p^i} V_{tb}^i(t)\, dt}}{\frac{1}{N_s} \sum_{j=1}^{N_s} \frac{\frac{2R_s}{c}}{\int_{\frac{2R_s}{c}+\tau_p^j}^{\tau_p^j} F_r^{-1}\{V_s^j(t)/G_s\}\, dt}} \qquad (20)$$

where the pulse indices i and j are now also necessary on the pulse duration τ_p for each shot, and the factors G_t in Equation (11) again cancel. If Equation (20) is inserted into Equation (7), we obtain the proper pulse-energy normalized, signal-averaged expression for $\langle \beta(R) \rangle$.

Often, however, normalization by the pulse energy is not done on a pulse-by-pulse basis, but rather the signal voltages and pulse energies are summed separately and the sums are divided at the end of the measurement. It is interesting to calculate the resultant errors due to this technique. We may generalize either the numerator or denominator of Equation (20) for this analysis and use a more convenient notation. Let the desired ensemble-average, including the pulse-by-pulse normalization, be given by

$$S = \frac{1}{N} \sum_{i=1}^{N} \frac{K_i}{E_i} \tag{21}$$

where K_i is the return "signal" and E_i is the pulse energy of the ith pulse. Let S′ be the incorrectly calculated ensemble-average as described above:

$$S' = \frac{\frac{1}{N} \sum_{i=1}^{N} K_i}{\frac{1}{N} \sum_{i=1}^{N} E_i} \tag{22}$$

If all the pulse energies E_i equal E_0, a constant, then S′ = S, and either technique is satisfactory. We now assume that $E_i = E_0 + \varepsilon_i$, where E_0 is the average pulse energy and ε_i represents the deviation of the ith pulse energy from E_0. Since it is obvious that S′ ≠ S for large pulse-energy fluctuations, we will assume the deviations are small, i.e., $\varepsilon_i \ll E_0$. If we insert the expression for E_i into Equation (21) we obtain

$$S = \frac{1}{N} \sum_{i=1}^{N} \frac{K_i}{(E_0 + \varepsilon_i)} = \frac{1}{N \cdot E_0} \sum_{i=1}^{N} K_i \left[1 - \left(\frac{\varepsilon_i}{E_0}\right) + \left(\frac{\varepsilon_i}{E_0}\right)^2 - \cdots \right] \tag{23}$$

and inserting it into Equation (22) gives

$$S' = \frac{\frac{1}{N} \sum_{i=1}^{N} K_i}{\frac{1}{N} \sum_{i=1}^{N} (E_0 + \varepsilon_i)} = \frac{1}{N \cdot E_0} \left(\sum_{i=1}^{N} K_i \right) \left[1 - \left(\frac{1}{N \cdot E_0} \sum_{i=1}^{N} \varepsilon_i \right) + \cdots \right] \tag{24}$$

Combining Equations (23) and (24) and using the fact that $\varepsilon_i/E_0 << 1$ and that $\langle \varepsilon_i \rangle = 0$, the fractional error is given approximately by

$$\frac{S'-S}{S} = \frac{\sum_{i=1}^{N} K_i \varepsilon_i}{E_0 \sum_{i=1}^{N} K_i} \tag{25}$$

Obviously, the error goes to 0 as ε_i/E_0 approaches 0. The size of the error will increase to the extent that K_i and ε_i are correlated. However, speckle and atmospheric turbulence will tend to reduce this correlation. Nevertheless, this source of error should be avoided by normalizing to pulse energy on a pulse-by-pulse basis.

4.3 RECTANGULAR PULSE ASSUMPTION

In Section 2.1 it was shown that Equation (2) was an exact expression for the aerosol backscatter power profile, $P_b(t)$, provided that the aerosol backscatter coefficient, $\beta(R)$, and the telescope overlap function, $O(R)$, were slowly varying with respect to the spatial distance $c\tau_p/2$. In going from Equation (2) to Equation (3), both the R^{-2} and exponential terms were removed from the integrand in order that the remaining integral would reduce to the transmitted pulse energy, an easily measured quantity. All terms removed from the integral in Equation (1) were assigned their values at the midpoint of the integration range, R_b. The rationale for this simplification often starts with the assumption that the transmitted pulse, $P_{tb}(t)$, is rectangular with power P_0 [W], duration τ_p, and therefore energy $P_0\tau_p$. Thus P_{tb} is removed immediately from the integral in Equation (2) and replaced with the constant P_0. At this point the range of integration is assumed to be narrow enough that the values at the midpoint, R_b, are used for the remainder of the integrand.

A careful look at Equation (2), however, reveals that the R^{-2} and exponential terms in the integrand combine to form a weighting function for the laser pulse profile $P_{tb}(t)$. This function favors the tail of the laser pulse (smaller R) in a complex way that depends on R, $\alpha_b(R)$, and τ_p. We have evaluated the percentage error in Equation (2) that results from assuming that the pulse shape is rectangular with power P_0 when the actual pulse shape consists of two rectangular sections of unequal power and duration, as shown in Figure 3. Keeping the total pulse duration constant at τ_p, we let the initial pulse power be P_1 [W] for τ_p/a seconds and then provide for a "tail" with power P_1/b for the remainder of the pulse. This bi-level pulse profile is a good approximation to the output profile of many pulsed lasers that exhibit an initial gain-switched spike followed by a lower-power, longer-lasting tail. The pulse energy is fixed at $P_0\tau_p$ by letting

$$P_1 = \left(\frac{ab}{a + b - 1}\right) P_0 \tag{26}$$

If a = b = 1, Equation (26) reduces to the rectangular pulse. Figure 3 shows the resultant percentage error vs. range for several values of the parameters (a,b), for the total pulse duration τ_p, and for a constant attenuation coefficient $\alpha_b(R) = 0.125\ km^{-1}$. It is clear that the percentage error can be very large, especially for large values of (a,b), that the error increases with increasing pulse duration, and that the error generally decreases with increasing range. Calculations using other values for α_b show that the percentage error is not strongly dependent on α_b. For example, with t = 5 μs, τ_p = 4 μs, and (a,b) = (8,8), where the error is large, letting α_b = 0.4, 0.125, and 0 km^{-1} yielded percentage errors of 72%, 68%, and 66%, respectively.

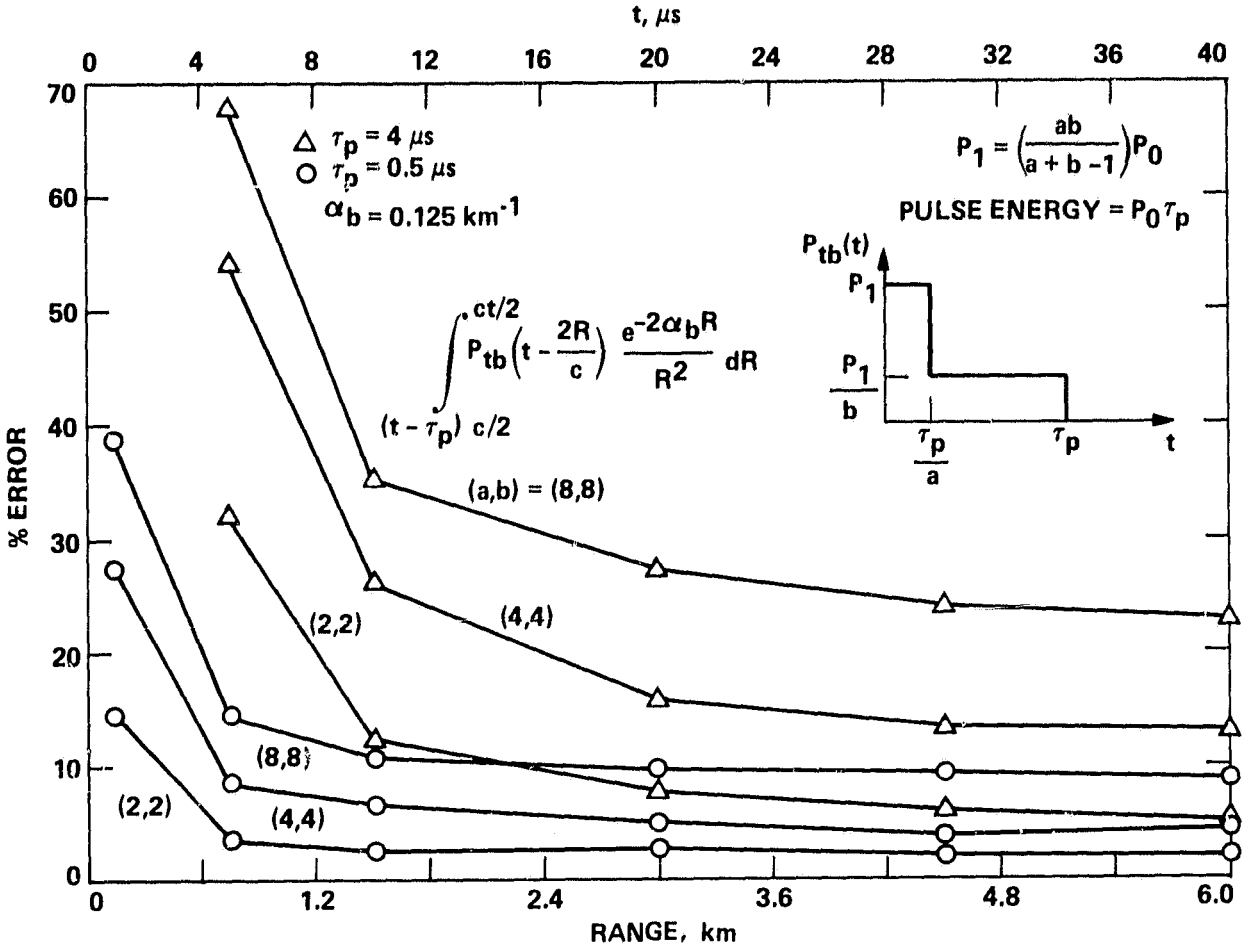

Figure 3. Calculated error vs. range due to the assumption of a rectangular transmitted-pulse profile when the actual profile is bi-level with duration τ_p and parameters a and b.

These results show that $\beta(R)$ will be overestimated by a range-dependent factor if Equation (3) is used. Only by using Equation (2), or correcting by the range-dependent factor, can this source of error be eliminated. Even if Equation (2) is used to solve for $\beta(R)$ by determining the pulse profile $P_{tb}(t)$ and the atmospheric extinction profile $\alpha_b(R)$, the return power profile $P_b(t)$ is not linearly proportional to pulse energy, making normalization to pulse energy very difficult. Only if the transmitted-pulse profile of each pulse were constant, so that $P_{tb}(t)$ could be written as the product of a pulse-energy term and a pulse-profile term, could Equation (2) be used to eliminate this "pulse-profile" source of error. Of course, both $\beta(R)$ and $O(R)$ may be varying significantly over distances of $c\tau_p/2$ and thus Equation (1) should be used, making the determination of $\beta(R)$ very difficult, since the profiles $\beta(R)$ and $\alpha_b(R)$ are both unknowns in the measurement.

SECTION 5

TELESCOPE OVERLAP FUNCTION

The range-dependent telescope overlap function, O(R), was introduced in Equations (1) and (5) as an important term that affects the received-power profile from both the atmospheric aerosol and hard targets. Essentially, O(R) is defined as the fraction of the transmitted pulse energy that is within the receiver's field-of-view. Obviously, factors that must be considered are the physical separation of the transmitting and receiving telescopes, their co-alignment or misalignment, the range-dependent spatial power profile of the transmitted beam, and the effective range-dependent spatial profile of the receiving telescope. Pulse-to-pulse variations in the transmitted spatial power profile would therefore produce pulse-to-pulse fluctuations in the telescope overlap function. The effective spatial profile of the receiver is due to many factors, including a central obstruction in the telescope, the finite size and shape of the detector element, sensitivity variations over the detector area, the variation in the position of the focal plane with range, and diffraction. For systems employing heterodyne detection, the local oscillator's spatial profile, polarization, and alignment at the detector plane must be considered.

Often the telescope overlap function is neglected in the lidar equation, especially when coaxial lidar systems are being analyzed. However, all of the factors contributing to O(R) for side-by-side lidar systems apply to coaxial systems except that the physical separation of transmitter and receiver is very small. Sassen and Dodd (1982) have analyzed the behavior of O(R) for both Gaussian and uniform transmitted-pulse profiles, and for various values of transmitter and receiver divergence, and transmitter-receiver misalignment. They have shown that O(R) is strongly dependent on alignment,

especially for typical lidar systems, which employ narrow transmitter and receiver beamwidths. Referring to Equation (1), we see that experimentally determining O(R) at a given wavelength requires that a very short rectangular laser pulse be fired into an atmosphere with well-known and slowly varying profiles $\beta(R)$ and $\alpha_b(R)$. Since this experiment would be difficult, a model for O(R) is usually used instead.

We have modeled the overlap function for the side-by-side telescope lidar system that is being used at JPL to measure the atmospheric aerosol backscatter coefficient in the troposphere in the 9 to 11 μm region (Kavaya et al., 1983). Figure 4 shows the modeled overlap function vs. range at the 10P(20) CO_2 laser wavelength (10.59 μm). The indicated parameters (X,Y) represent the position (misalignment) of the detector element in thousandths of an inch (mils) with respect to the optical axis, which is parallel to the transmitted pulse, and lying in the focal plane ($R = \infty$) of the receiver. Therefore, (X,Y) = (0,0) represents exact centering of the detector on the optical axis and (X,Y) = (-5,0) represents a 5-mil (127-μm) movement of the detector from the centered position. A 5-mil displacement is equivalent to a 0.074-mrad angular misalignment. The centers of the 15.5-cm diameter transmitter and receiver telescopes in our lidar system are displaced by 25.5 cm in the "X" direction and 7.3 cm in the "Y" direction. For our sign convention, negative values of X result in the crossing of the transmitter and receiver optical axes at some positive range from the telescopes. This range is indicated in Figure 4 for the appropriate curves. Note that the peak of these "negative X" curves does not occur at the crossover range but that the largest overlap function value at any range is given by the curve corresponding to that crossover range. The finite size (300 μm square) of the detector is

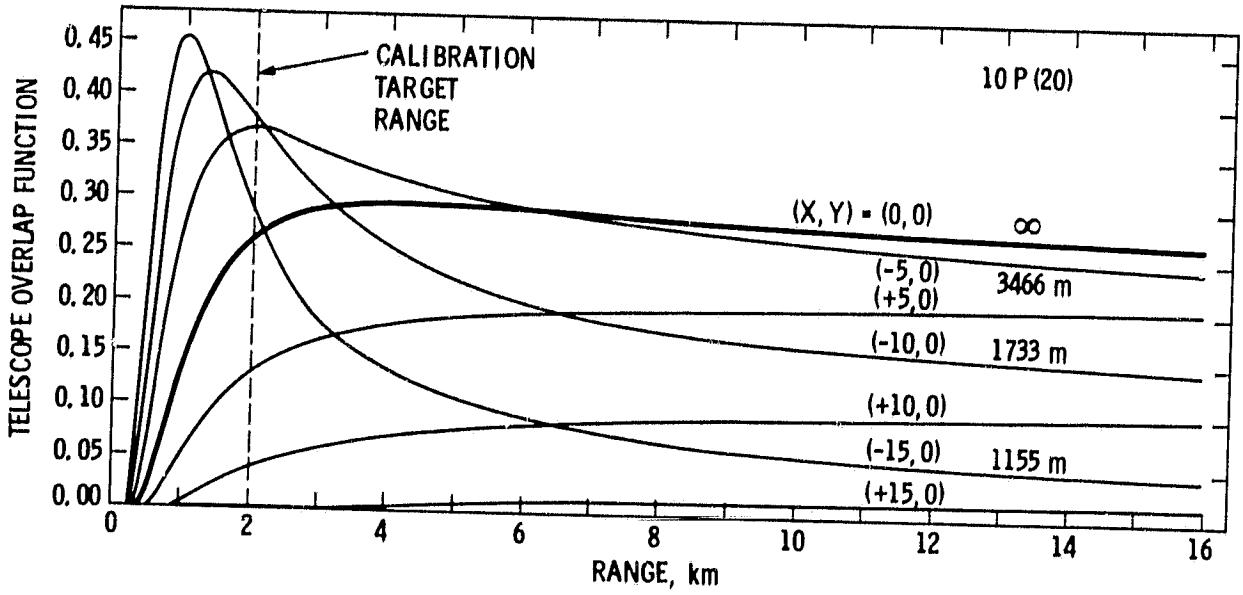

Figure 4. Modeled telescope overlap function of the JPL lidar system vs. range at the 10P(20) CO_2 laser line as a function of various detector positions (in mils) with respect to the optical axis and lying in the receiver focal plane.

accounted for by averaging the center and four corner positions of the detector. In addition to assuming uniform detector responsiveness and using the five-point average, we make other assumptions in the model, including that there is a uniform local oscillator, negligible receiver focal plane variation with the range beyond R_{MIN} = 1.1 km, and a uniform, circular, transmitted-pulse spatial profile that diffracts at 150% of the diffraction limit. Although these assumptions limit the accuracy of the model, experimental results obtained by firing the lidar system with various values of (X,Y) agree quite well with the curves in Figure 4 and also allow determination of the optimum (0,0) detector position.

It is clear from Figure 4 that the overlap function varies significantly with very small detector misalignments. Not only is it important to know O(R) when reducing the aerosol backscatter power profile, but it is especially important when using a hard target for calibration. A common range used with our calibration target is 2 km, which is indicated in Figure 4. The calculation of β at any range R will involve the ratio of the telescope overlap function at the target's range, R_s, to its value at R as is shown in Equation (7). It is clear from the curves in Figure 4 that assuming an incorrect telescope overlap function (or neglecting it) can cause significant errors in calculating $\beta(R)$. For example, when the system is perfectly aligned, i.e., when (X,Y) = (0,0), then the ratio of the overlap function's value at 16 km to its value at 2 km is approximately 1. However, if the system were misaligned by only 220 μrad, e.g., (X,Y) = (-15,0), then the same ratio is approximately 6. If correct alignment was mistakenly assumed, or if the telescope overlap function was neglected, then a ratio of 1 would be used and the value of β(16 km) would be overestimated by a factor of 6.

An additional problem in determining O(R) occurs with airborne lidar systems. This is due to the fact that once the laser pulse is transmitted, the receiver telescope will move with respect to its t = 0 position. Since calibration of the system with a hard target is most convenient on the ground before takeoff, the overlap function for the stationary lidar system will not apply to the moving (airborne) lidar system. Fortunately, the sensitivity of O(R) to the displacement of the receiver will be greatest at short ranges, where the displacement will be the least. Whether the system is airborne or not, the telescope overlap function of every lidar system should be modeled as accurately as possible at each wavelength of interest and checked experimentally.

SECTION 6

HARD-TARGET CALIBRATION

The hard-target parameter ρ^* was introduced in Equation (5) as the power reflected from the hard target per steradian towards the receiver, divided by the incident power. As is clear from Equation (7), a quantitative evaluation of this parameter is required to calculate $\beta(R)$ when hard-target measurements are being used for calibration. It has been shown (Kavaya et al., 1983) that the evaluation of ρ^* for a given calibration target, lidar wavelength, and lidar geometry is not trivial. Although hard targets are frequently used to calibrate lidar systems, there is a surprising lack of published information about their reflectance properties. The derivation of ρ^* and a technique for its evaluation will be outlined in this section.

The geometric reflectance properties of a flat, uniform, isotropic surface can be described by the bidirectional reflectance-distribution function (BRDF) [sr^{-1}] defined by Nicodemus et al. (1977) as

$$f_r(\Theta_i,\phi_i;\Theta_r,\phi_r) = \frac{dL_r(\Theta_i,\phi_i;\Theta_r,\phi_r;E_i)}{dE_i(\Theta_i,\phi_i)} \tag{27}$$

In Equation (27) L_r is the reflected radiance [$W\ m^{-2}\ sr^{-1}$] in the direction (Θ_r,ϕ_r) due to the incident irradiance $dE_i = L_i \cos\Theta_i\ d\omega_i$ [$W\ m^{-2}$] confined to the solid-angle element $d\omega_i$ in the direction (Θ_i,ϕ_i); Θ is the polar angle between the ray and the average surface normal; ϕ is the azimuthal angle between the ray's projection in the surface and a reference direction in the surface; and the subscripts i and r on L, E, Θ, and ϕ refer to the incident and reflected radiation, respectively. The radiance in the direction (Θ,ϕ) is defined by

$$L(\Theta,\phi) = \frac{d^2\Phi}{dA\ \cos\Theta\ d\omega} \tag{28}$$

where $d^2\phi$ is the element of radiant flux [W] through the element of area dA in the direction (Θ,ϕ) and within the solid-angle element $d\omega$. The element of the projected area perpendicular to the ray direction (Θ,ϕ) is $dA\cos\Theta$. Equation (27) does not treat interference, diffraction, transmission, absorption, fluorescence, or polarization effects, and it is assumed that the illumination is monochromatic, uniform, and isotropic. The BRDF is an unmeasurable derivative capable of values from 0 to infinity. Real measurements always involve an average of f_r over finite intervals, e.g., $\Delta\omega$ and $\Delta\lambda$.

Nicodemus et al. (1977) define nine reflectances, allowing for directional, conical, or hemispherical geometry of the illuminating and reflected radiation. The most basic quantity, the biconical reflectance, is defined as

$$\rho(\omega_i;\omega_r) = \frac{\int_{\omega_r}\int_{\omega_i} f_r(\Theta_i,\phi_i;\Theta_r,\phi_r)\cos\Theta_i\cos\Theta_r\, d\omega_i\, d\omega_r}{\int_{\omega_i}\cos\Theta_i\, d\omega_i} \tag{29}$$

where $\rho(\omega_i;\omega_r)$ is the ratio of the radiant flux in the direction (Θ_r,ϕ_r) within ω_r to the incident flux in the direction (Θ_i,ϕ_i) within ω_i. (We will avoid the use of the projected solid angle $d\Omega = \cos\Theta\, d\omega$ as it is nonphysical and can lead to confusion.) A Lambertian (diffuse) surface is one for which the reflected radiance is isotropic (L_r is constant, independent of Θ_r and ϕ_r) regardless of how it is irradiated, and thus its BRDF, $f_{r,d}$, is necessarily a constant. From Equation (29) we see that

$$f_{r,d}(\Theta_i,\phi_i;\Theta_r,\phi_r) = \rho(\omega_i;2\pi)/\pi \tag{30}$$

If the solid angle ω_i confining the illuminating radiation is small enough that we can consider f_r to be constant over the limits of integration, Equation (29) reduces to

$$\rho(\Theta_i,\phi_i;\omega_r) = \int_{\omega_r} f_r(\Theta_i,\phi_i;\Theta_r,\phi_r)\cos\Theta_r\, d\omega_r \tag{31}$$

which is the directional-conical reflectance, i.e., the illuminating radiation is from a specific direction, and the reflected radiation is measured in a cone of solid angle ω_r. The reflectance measured by an ideal integrating sphere, ρ_{IS}, is given by Equation (31) with $\omega_r = 2\pi$,

$$\rho_{IS} = \rho(\Theta_i,\phi_i;2\pi) = \int_0^{2\pi}\int_0^{\pi/2} f_r(\Theta_i,\phi_i;\Theta_r,\phi_r)\cos\Theta_r \sin\Theta_r\, d\Theta_r\, d\phi_r \tag{32}$$

which is the directional-hemispherical reflectance. If the small ω_i assumption is not valid, Equation (29) should be used for ρ_{IS} with $\omega_r = 2\pi$. If the monochromatic illumination assumption is not true, an average over $\Delta\lambda$ will be measured. The common term albedo is the hemispherical-hemispherical reflectance, i.e., $\rho(2\pi;2\pi)$.

In lidar applications both the illuminating and receiving solid angles are very small. For example, a 15-cm diameter telescope subtends only 7.1×10^{-8} sr at a range of 500 m. Thus we may further simplify Equation (31) by letting $\omega_r \to 0$, yielding

$$\rho(\Theta_i,\phi_i;\Theta_r,\phi_r) = \omega_r \langle f_r(\Theta_i,\phi_i;\Theta_r,\phi_r)\rangle \cos\Theta_r \tag{33}$$

where $\langle f_r\rangle$ is the average value of f_r over the finite solid-angle intervals ω_i and ω_r.

From Equation (33) it may be concluded that the received power from a Lambertian target (f_r = constant) will vary as $\cos\theta_r$. However, this conclusion is not always correct. It is important to consider the relative sizes of the target, the illuminated area on the target, and the area of the target viewed by the detector, as shown in Figure 5.

Recall that in Equation (33), ρ is the ratio of the reflected flux to the incident flux. The incident flux is not necessarily constant but is given by the product of the power per illuminated target area and the viewed illuminated target area. Figure 5a depicts the similar cases $A_i < A_r < A_s$ or $A_i < A_s < A_r$, where $A_i = A_{io}/\cos\theta_i$ is the area illuminated by a laser with constant power P, $A_r = A_{ro}/\cos\theta_r$ is the area viewed by the detector, and A_s is the target area. Note that the illuminated spot is smallest in this case, and, therefore, θ_i may not approach 90°. The power per illuminated target area is given by $P\cos\theta_i/A_{io}$, and the viewed illuminated target area is given by $A_{io}/\cos\theta_i$. Thus the $\cos\theta_i$ terms will cancel, leaving only the $\cos\theta_r$ dependence of ρ in the expression for received power. In Figure 5b we have the cases $A_r < A_i < A_s$ or $A_r < A_s < A_i$; the receiver field-of-view at the target is smallest. Here the power per illuminated target area is again given by $P\cos\theta_i/A_{io}$, but the viewed illuminated target area is now given by $A_{ro}/\cos\theta_r$. When these angular dependences are combined with Equation (33), we see that the overall dependence of the received power is given by $\cos\theta_i$. As seen in Figure 5, when a collinear backscatter (e.g., lidar) geometry is considered with $\theta_i = \theta_r = \theta$, all the above cases exhibit a $\cos\theta$ dependence. Finally, Figure 5c depicts the cases $A_s < A_i < A_r$ or $A_s < A_r < A_i$; the target area is smallest. Once again the power per illuminated target area is $P\cos\theta_i/A_{io}$, but the viewed illuminated target area is just A_s. When these

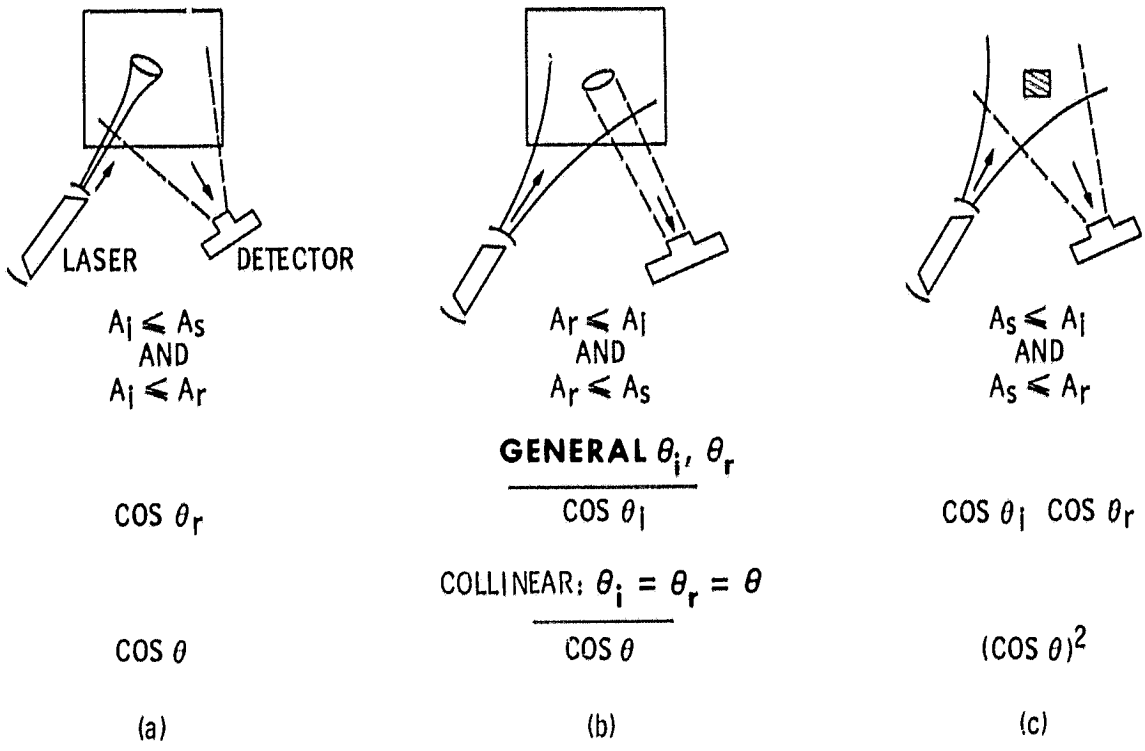

Figure 5. Pictorial representation of three possible reflectance geometries: (a) the illumination area at the target is smaller than both the target and the detector field-of-view at the target, (b) the field-of-view of the detector is smallest, and (c) the target area is smallest.

factors are combined with Equation (33), we obtain a $\cos\Theta_i\cos\Theta_r$ dependence. In this case the collinear geometry yields a $(\cos\Theta)^2$ dependence. Of course, a more complicated geometry than those cases in Figure 5 is possible; e.g., if A_i, A_r, and A_s have boundaries that cross each other. It is clear that the geometry of any reflectance experiment is very important, especially when laboratory target reflectance data are used to characterize targets, which are in turn placed in a lidar geometry for calibrating lidar systems. Seldom in the literature is the geometry of a reflectance experiment defined in terms of the cases of Figure 5. The Lambertian reflectance behavior is predominantly given as $\cos\Theta_r$ (small A_i), although examples of $\cos\Theta_i\cos\Theta_r$ (small A_s) can be found as well as examples of $\cos\Theta_i$ (small A_r), especially in astronomy.

Later in this section we will discuss target measurements using a cw CO_2 laser in a collinear backscatter geometry ($\Theta_i = \Theta_r = \Theta$), where $A_i \sim A_r < A_s$. These measurements provide collinear Θ dependence of each target's reflectance, showing various deviations from Lambertian ($\cos\Theta$) dependence. It is tempting to assume that each target's Θ dependence curve could be scaled absolutely by using integrating-sphere data and the area under the Θ dependence curve. However, this is not possible for surfaces with a general BRDF. The integrating-sphere data depend on the BRDF, as shown in Equation (32), while the backscatter data will depend on Θ_r, as shown in Equation (33):

$$S(\Theta_r') \propto \omega_r' \langle f_r(\Theta_i',\varphi_i';\Theta_r',\varphi_r')\rangle \cos\Theta_r' \tag{34}$$

where primes are used to differentiate from the angles in the integrating-sphere case. We may let $\Theta_i' = \Theta_r' = \Theta$ and $\phi_i' = \phi_r' = \phi_i$, where we use the

collinear geometry and the assumed isotropic property of the target (f_r independent of ϕ_i). If we now multiply $S(\Theta)$ by $\sin\Theta$ and integrate over Θ, we obtain

$$I = \int_0^{\pi/2} S(\Theta) \sin\Theta \, d\Theta \propto \omega_r' \int_0^{\pi/2} \langle f_r(\Theta,\phi_i;\Theta,\phi_i)\rangle \cos\Theta \sin\Theta \, d\Theta \qquad (35)$$

In comparing Equations (32) and (35) we see that we may not use ρ_{IS} to ...le $S(\Theta)$ unless certain conditions hold. First, the backscatter experiment's solid angles must be small enough to allow the assumption that $\langle f_r \rangle = f_r$. Second, f_r must be independent of ϕ_r to allow the parameter ϕ_r of f_r in Equation (32) to be set equal to ϕ_i. Finally, f_r must be independent of Θ_i to allow the parameter Θ_i in Equation (32) to be set equal to Θ_r. Under these conditions the integrals of Equations (32) and (35) are proportional to each other. However, the requirement that $f_r(\Theta_i,\phi_i;\Theta_r,\phi_r)$ be independent of Θ_i, ϕ_i, and ϕ_r is nearly as restrictive as the Lambertian assumption of constant f_r (i.e., independent of all four parameters).

It is common to find expressions in the literature that give the parameter ρ^* as either ρ, ρ/π, or $(\rho \cos\Theta)/\pi$, where ρ is called the "reflectivity" of the target. If the BRDF of a calibration target is sufficiently known, we may more exactly define ρ^*. Under the assumptions leading to Equation (29), e.g., uniform and isotropic illumination and target surface, we see that the general expression for ρ^* in Equations (5) and (7) is

$$\rho^*(\omega_i;\omega_r) = \frac{\int_{\omega_r} \int_{\omega_i} f_r(\Theta_i,\phi_i;\Theta_r,\phi_r) \cos\Theta_i \cos\Theta_r \, d\omega_i \, d\omega_r}{\omega_r \int_{\omega_i} \cos\Theta_i \, d\omega_i} \qquad (36)$$

If small solid angles can be assumed, Equation (36) becomes

$$\rho^*(\Theta_i,\phi_i;\Theta_r,\phi_r) = \langle f_r(\Theta_i,\phi_i;\Theta_r,\phi_r)\rangle \cos\Theta_r \tag{37}$$

and if collinear geometry is used, Equation (37) becomes

$$\rho^*(\Theta,\phi;\Theta,\phi) = \langle f_r(\Theta,\phi;\Theta,\phi)\rangle \cos\Theta \tag{38}$$

If the geometry of Figure 5c applies, $\cos\Theta$ is replaced by $(\cos\Theta)^2$ in Equation (38). If the target is Lambertian (diffuse), then Equation (38) becomes

$$\rho^*(\Theta,\phi;\Theta,\phi) = \frac{\rho(\omega_i;2\pi)}{\pi}\cos\Theta = \frac{\rho_{IS}}{\pi}\cos\Theta \tag{39}$$

It is apparent that considerable calibration error may result from replacing ρ^* in Equation (5) or (7) with either ρ, ρ/π, or even $(\rho\cos\Theta)/\pi$ when the experimental geometry resulting in the reported value of ρ is unknown; when the center wavelength, bandwidth, and polarization of the illumination may have differed from that in use; and when the target surface is most likely not Lambertian or reproducible.

The ideal calibration target would have a well-known BRDF and would be inexpensive, easy to fabricate, durable, and reproducible. It has been shown that quantitative characterization of a target using integrating-sphere data and laboratory backscatter Θ dependence data is only possible if $f_r(\Theta_i,\phi_i;\Theta_r,\phi_r)$ is independent of Θ_i, ϕ_i, and Θ_r, a very restrictive condition that is satisfied by Lambertian surfaces. Thus, a Lambertian target possessing the qualities listed above would greatly facilitate the calibration process.

If the reflected radiation of a Lambertian target were measured using a collinear backscatter geometry ($\theta_i = \theta_r = \theta$) with $A_i \sim A_r < A_s$, then Equation (39) predicts a $\cos\theta$ signal dependence as θ is varied. The lack of a $\cos\theta$ signal dependence would indicate that a hard target was not Lambertian, while the presence of a $\cos\theta$ dependence would strongly indicate that the target was Lambertian. We have fabricated a collinear backscatter apparatus at JPL, which uses a cw CO_2 laser for illumination wavelengths in the 9 to 11 μm region, to investigate candidate calibration target surfaces (Kavaya et al., 1983). The laboratory collinear backscatter apparatus is shown in Figure 6. The passively stabilized, linearly polarized, cw CO_2 laser is grating-tunable in the 9 to 11 μm region. The laser radiation was chopped at 100 Hz and was directed onto both the target surface and a power meter with a ZnSe beam-splitter. The vertical polarization of the laser was perpendicular to the plane of incidence at the target. A 30-cm focal length, 5-cm diameter BaF_2 lens was used to image the target surface onto an LN_2-cooled, HgCdTe infrared detector. A preamplifier and lock-in amplifier (not shown) were then used to obtain the signal magnitude. A ZnSe polarizer that had a greater than 500:1 extinction ratio and 10-mm diameter aperture was positioned next to the detector and was used to select backscattered radiation with polarization either parallel or perpendicular to that of the illuminating beam. (The different reflection coefficients of the beam-splitter for the two directions of polarization were measured, and the data were appropriately scaled.) The target was carefully positioned to align the center of illumination with the axis of rotation. The beam size at the target was ~5 mm in diameter and was smaller than the target even at $\theta = 80^\circ$. Since backscatter from the power meter contributed a large background signal, the power meter was

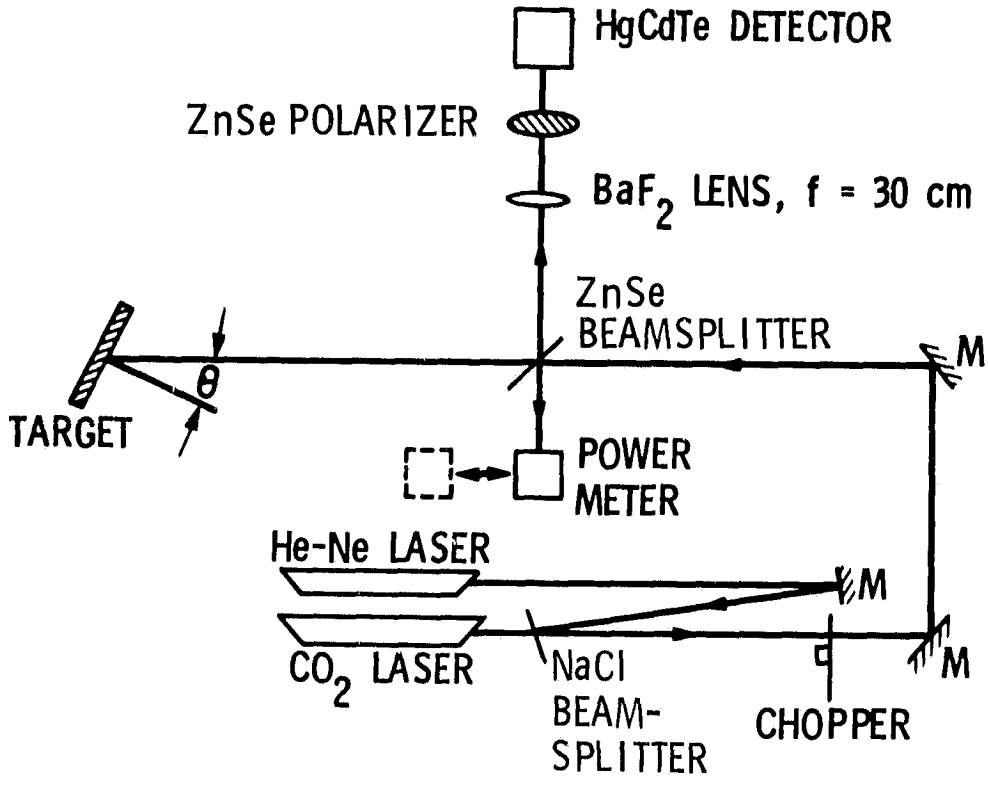

Figure 6. Laboratory collinear backscatter apparatus.

removed during measurements, and the unblocked beam was allowed to travel several meters before scriking anything. Background readings were then taken with a mirror that was placed between the beam-splitter and the target, and that also directed that beam across the laboratory. The background readings were found to be negligible. The data were normalized by the laser power. The finite size of the lens limited the resolution in Θ to 3.2^{o}. However, it did help reduce the signal fluctuations due to speckle, with an estimated 100 speckle lobes being averaged. Speckle effects were further reduced by averaging several measurements within $\pm 0.5^{o}$ of the desired value of Θ. Later, a spinning target was incorporated to essentially eliminate the speckle effects.

We chose four target surfaces for this work: sublimed flowers of sulfur (S), flame-sprayed aluminum (FSA), 20-grit sandblasted aluminum (SBA), and 400-grit silicon carbide sandpaper (SC). The sulfur target was fabricated by mixing sublimed sulfur (J.T. Baker 4088) with acetone to form a slurry ($\sim$ 1.4 g sulfur to 1 ml acetone). The slurry was packed into a rectangular well that was machined in aluminum to a 4.4-mm depth. A microscope slide lubricated with acetone was used to trowel a uniform surface finish that appeared smooth to the naked eye. The target was then allowed to dry overnight. The flame-sprayed aluminum target was made by sandblasting 6061 aluminum plate with 60-grit sand, priming with Ni alumina bonding agent, and finally flame-spraying with pure aluminum to a thickness of 0.25 to 0.38 mm. The measurements (Kavaya et al., 1983) showed that the FSA, SBA, and SC targets all deviated significantly from the Lambertian $\cos\Theta$ dependence, whereas the flowers-of-sulfur target obeyed the $\cos\Theta$ dependence within our experimental uncertainty. The worst deviations occurred with the SC target, whose signal was fairly independent of Θ, indicating that retroreflection was responsible.

If we let the symbol s represent the backscattered radiation with polarization perpendicular to the illumination polarization direction, and p represent the backscattered component parallel to the illumination, then the depolarization ratio, defined as s/(p + s), varied from approximately 10% to 30% for the four targets. The largest depolarization ratio corresponded to the flowers of sulfur, which is consistent with the idea that Lambertian behavior is caused by multiple subsurface scattering. The preservation of polarization direction with specular reflection was supported by the fact that the FSA and SBA targets exhibited specular reflection components near $\theta = 0^{o}$ only in their parallel backscatter profiles and not in their perpendicular backscatter profiles, and by the fact that the depolarization ratio of the "retroreflecting" SC target was the lowest (~10%).

Although our measurements indicated that the flowers-of-sulfur target was Lambertian at λ = 9.6 and 10.6 μm, and presumably also at other CO_2 laser wavelengths, it is not an ideal calibration target. Our lidar beamwidths and calibration target range (2 km) require a large target surface (~1.8 m square) that is durable enough for field use. The sulfur targets, however, are very fragile and inconvenient to make in large sizes. We have found that the smooth surface appearance is required for the Lambertian behavior. Also, little is known about the effects of aging or exposure on the BRDF of the sulfur.

To take advantage of the Lambertian behavior of the sulfur, we have adopted a primary and secondary standard-calibration technique. A flowers-of-sulfur target, which exhibits Lambertian behavior, is made the primary standard. An integrating sphere is then used to measure the directional-hemispherical reflectance, ρ_{IS}, of the target as a function of wavelength

with an incident illumination angle of 45^{o} (Kavaya et al., 1983). Since Equation (39) applies to the sulfur target, ρ^* may be calculated for any angle Θ. A large, durable FSA target is then fabricated and made the secondary standard. This target is used in the field with $\Theta = 45^{o}$ as the lidar calibration target. Assuming homogeneity, a small piece of the FSA target, suitable for use in the apparatus of Figure 6, is cut off.

Using the apparatus shown in Figure 6, a ratio of backscatter reflectance is determined between the primary sulfur target and the secondary FSA target. This ratio is measured at $\Theta = 45^{o}$, with the incident and detected directions of polarization matched to that of the lidar geometry, and at each wavelength of interest. Finally, the value of ρ^* for sulfur, calculated from Equation (39), is multiplied by the measured reflectance ratio of FSA to sulfur, to obtain the ρ^* for FSA that is inserted into Equation (7). For example, we have used this technique to determine a value of 0.097 for ρ^* of our FSA lidar calibration target at the 10P(20) CO_2 laser wavelength. If FSA is assumed to be Lambertian, however, with a "reflectivity" of 80%, which has been done in the literature, then the calculated value of ρ^* would be $0.8 \cos 45^{o}/\pi = 0.18$. This value is 86% larger than our value.

Ideally, the reflectance transfer from the primary to the secondary standard should be done under conditions that match both the integrating-sphere measurement and the lidar measurement as closely as possible. In practice, however, there are many departures from this ideal. The transfer angle, Θ, should match the incident angle in the integrating-sphere measurements and the lidar-target polar angle. The solid angles ω_i and ω_r in all three measurements should be as close as possible. (This may be impractical since lidar solid angles are so small. Thus the BRDF of the

primary and secondary targets should not vary strongly with Θ. This consideration makes retroreflecting targets a poor choice.) The sensitivity of the reflectance transfer ratio to ω_i and ω_r could be studied by varying the solid angles in the backscatter apparatus. A tunable cw CO_2 laser should serve as the illumination source for the integrating-sphere data with polarization geometry identical to the other two measurements. (If the integrating-sphere measurements of sulfur are made with unpolarized light, then four measurements of the sulfur at $\Theta = 45^{\circ}$ should be made with the collinear backscatter apparatus. A measurement should be taken with all four permutations of parallel and perpendicular, incident and reflected radiation: ss, sp, pp, and ps. One-half of the sum of these four readings should then be ratioed with the single (e.g., ss) reading of the FSA target.) The same Lambertian sulfur target should be used for both the integrating-sphere and transfer measurements. The secondary target should be as homogeneous as possible so that the small piece used in the transfer measurement accurately represents the larger lidar target. (We have seen variations in the BRDF of different FSA targets that probably are due to the operator, the fabrication technique, the size of the target, etc.) In addition, the small piece cut from the secondary target should be kept with the larger target, and thus be subjected to the same environment, so that later transfer measurements can be used to update the calibration and to study aging and exposure effects.

It has been shown that the calibration-target parameter ρ^*, which must be well-known for accurate calibration of aerosol backscatter data, depends intimately on the BRDF of the target surface, a function that can only be partially measured with a costly, time-consuming, and complex goniometric experimental measurement and that likely varies with the wavelength, polarization, and bandwidth of the illuminating radiation, and with the subtended solid

angles of the illumination and detector. Little is known about the variations of the BRDF of hard targets with these parameters, or the variations with time and exposure for a single target, or the variations among different samples of the same type of target surface. It appears at present that the best method for determining the value of ρ^* for the lidar equation is to use the primary and secondary standard technique outlined above, including consistent and coordinated integrating-sphere, collinear backscatter reflectance ratio, and lidar measurements.

SECTION 7

ATMOSPHERIC MODELING

The remaining two parameters of Equation (7) that must be known in order to calculate $\beta(R)$ are $\alpha_s(R)$ and $\alpha_b(R)$, the atmospheric extinction profiles for the optical paths from the lidar to the hard target and aerosol particles, respectively. Ideally, both profiles would be accurately measured at the time of each lidar measurement and at the transmitted wavelength. Unfortunately, this is very difficult to do. It is clear from Equation (2) that the lidar signal does not readily yield the atmospheric extinction profile when $\beta(R)$ and $\alpha_b(R)$ are both unknowns. An analytic relationship between β and α_b is not possible at 10 μm since the extinction is mainly molecular while the backscatter is due to the aerosol particles. However, if the pulse duration τ_p is sufficiently short, if the overlap function $O(R)$ is well-known, and if both $\beta(R)$ and $\alpha_b(R)$ can be assumed to be independent of R, then the lidar signal in Equation (2) can be used to determine the extinction coefficient. These conditions are reasonable for horizontal paths if both β and α depend only on altitude. Thus the extinction profile $\alpha_s(R)$ may be considered to be constant if a horizontal path between the lidar and the calibration target is employed. Furthermore, by aiming the lidar so that it just misses the target, and therefore obtaining backscatter from a much longer yet similar horizontal path, the value of $\alpha_s(R) = \alpha_s$ may be determined. For a ground-based lidar, such as the coherent CO_2 lidar at JPL, the horizontal path lies in the boundary-layer and α_s is called the boundary-layer total attenuation α_{BL}.

These steps are shown in Figure 7 in relation to the overall calibration process used at JPL to reduce the lidar backscatter data and

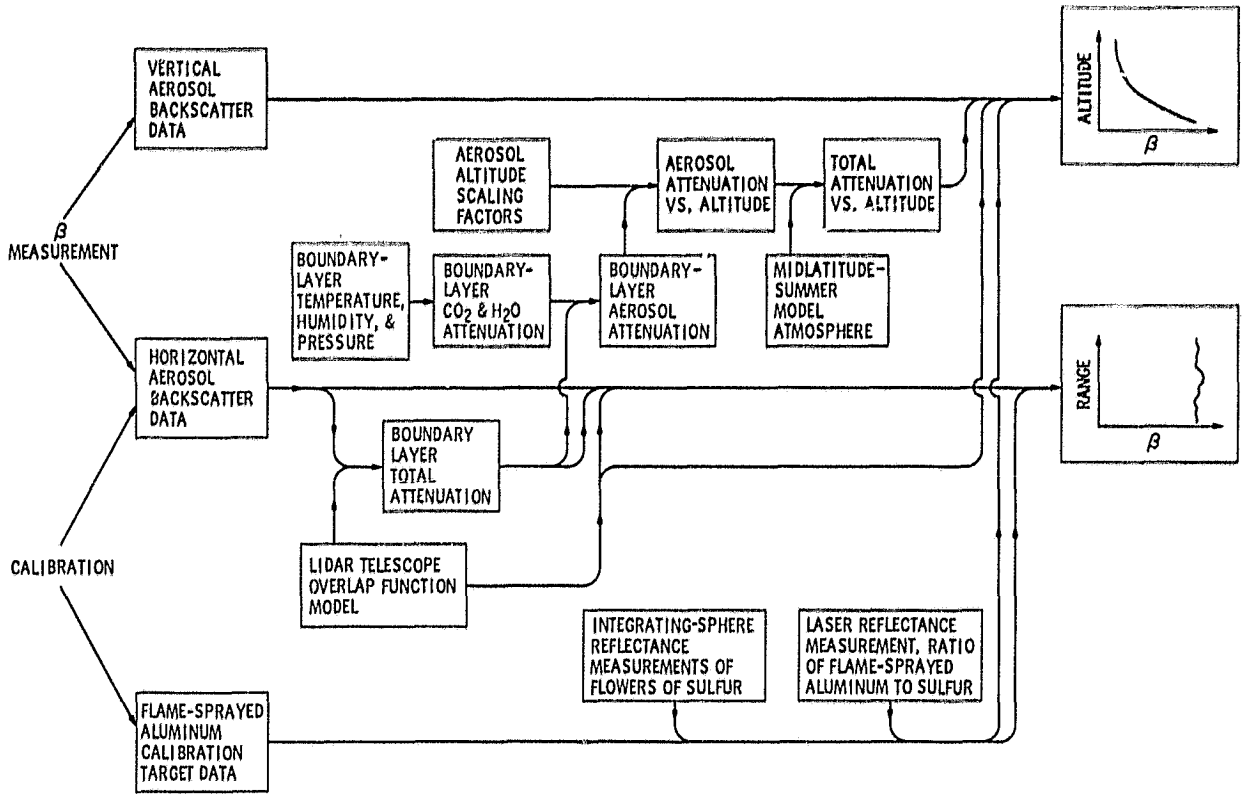

Figure 7. Flow diagram depicting the main components in the lidar calibration and β profile computation.

calculate vertical and horizontal β profiles from vertical and horizontal aerosol backscatter data and from horizontal hard-target backscatter data. Note that the steps of data acquisition and data processing, as discussed in Sections 3 and 4, are not portrayed in Figure 7. However, both the telescope overlap function and hard-target calibration, discussed in Sections 5 and 6, are shown in the calibration flow diagram.

Obtaining the extinction profile $\alpha_b(R)$ for the vertical aerosol backscatter data is much more difficult than obtaining $\alpha_s(R)$. Equation (2) may not be used, since both $\alpha_b(R)$ and $\beta(R)$ will depend on R. Direct measurement of extinction vs. height at the transmitted wavelength and at the time of each measurement would be very difficult and expensive. At CO_2 laser wavelengths the total extinction consists of molecular extinction and aerosol extinction. If the CO_2 line is chosen to avoid resonances of trace species such as ozone, then the molecular extinction will be due primarily to CO_2 and water vapor. The extinction due to these two molecules may be calculated from altitude profiles of atmospheric temperature, pressure, and relative humidity. These profiles may be measured directly using rawinsonde or radiosonde ascent probes. An alternative to the inconvenience and cost of ascent probes is to use a model for the atmospheric temperature, pressure, and relative humidity that is appropriate to the measurement location and season. As shown in Figure 7, this latter technique is used at JPL. The molecular attenuation vs. altitude above the boundary layer is calculated using the Midlatitude-Summer model profiles for temperature and water vapor (McClatchey et al., 1972), the CO_2 and H_2O absorption-line parameters from the 1982 AFGL atmospheric absorption-line parameter compilation (Rothman et al., 1983), and the water-vapor continuum absorption parameters given in LOWTRAN 5 (Kneizys et al., 1980).

Figure 8 shows the calculated molecular attenuation for various CO_2 laser lines. Within the boundary layer the total attenuation calculated from the horizontal aerosol backscatter is used. (A slant-path aerosol backscatter measurement through the boundary layer may also be employed to determine the height of the boundary layer.) The molecular (CO_2 + H_2O) contribution to the boundary-layer attenuation is calculated from direct measurements of temperature, relative humidity, and pressure. This is subtracted from the total boundary-layer attenuation to obtain the aerosol contribution in the boundary layer. The aerosol attenuation normally decreases rapidly with increasing altitude above the boundary layer. A model for the aerosol altitude scaling factors (McClatchey and D'Agati, 1978) is used to derive the aerosol contribution to attenuation vs. altitude. These altitude scaling factors are also shown in Figure 8. Finally, the total attenuation vs. altitude $\alpha_b(R)$ (see Figure 7) is found by adding the aerosol and molecular contributions.

Any errors in the two profiles, $\alpha_s(R)$ and $\alpha_b(R)$, that are used in Equation (7) will obviously produce errors in the calculated profile $\beta(R)$. If we let $\alpha_s(R)$ and $\alpha_b(R)$ represent the true atmospheric profiles, and $\alpha_s'(R)$ and $\alpha_b'(R)$ represent incorrect profiles that are used in Equation (7) to calculate $\beta'(R)$, then the ratio of incorrect to correct β is given by

$$\frac{\beta'(R_b)}{\beta(R_b)} = \frac{\exp\left\{-2\int_0^{R_s}\alpha_s'(R')dR'\right\}}{\exp\left\{-2\int_0^{R_s}\alpha_s(R')dR'\right\}} \times \frac{\exp\left\{-2\int_0^{R_b}\alpha_b(R')dR'\right\}}{\exp\left\{-2\int_0^{R_b}\alpha_b'(R')dR'\right\}} \qquad (40)$$

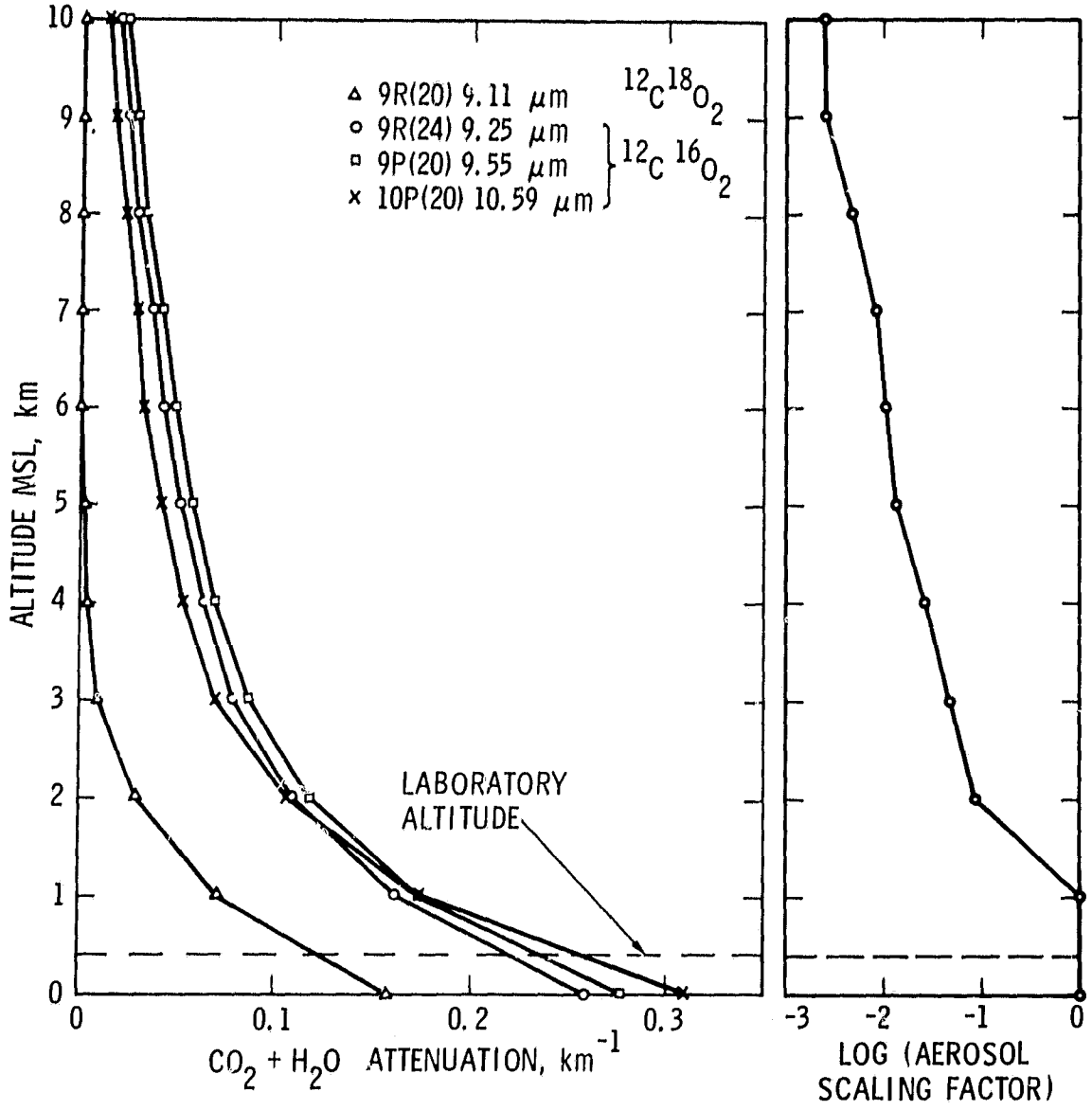

Figure 8. Molecular attenuation and aerosol extinction scaling factor profiles that are used above the boundary layer for computation of the total attenuation. A Midlatitude-Summer model of atmospheric pressure, temperature, and relative humidity was used. The attenuation at 9.11 μm, which is not significantly affected by atmospheric carbon dioxide, is shown for comparison.

The ratio given by Equation (40) may be applied to the typical atmospheric modeling geometry shown in Figure 9. We let the lidar system fire into the atmosphere at zenith angle Θ from altitude Z_L. The atmosphere is modeled by layers i that have total attenuation α_i and an upper altitude of Z_i. When appropriate, the first layer is the boundary layer with attenuation $\alpha_1 = \alpha_{BL}$ and altitude $Z_1 = Z_{BL}$. The horizontal path to the calibration target is in the first layer, and the altitude Z at which β is being calculated is assumed to lie in layer j. With this geometry, Equation (40) becomes

$$\frac{\beta'(R_b)}{\beta(R_b)} = \exp\left\{-2 k_s(\alpha'_{BL} - \alpha_{BL})\right\} \exp\left\{-\frac{2}{\cos\Theta}\left[\alpha_{BL} Z_{BL} - \alpha'_{BL} Z'_{BL} + Z_L(\alpha'_{BL} - \alpha_{BL})\right]\right\}$$

$$\times \exp\left\{-\frac{2}{\cos\Theta}\left[\alpha_2(Z_2 - Z_{BL}) - \alpha'_2(Z'_2 - Z'_{BL})\right]\right\} \times \cdots$$

$$\times \exp\left\{-\frac{2}{\cos\Theta}\left[\alpha_{j-1}(Z_{j-1} - Z_{j-2}) - \alpha'_{j-1}(Z'_{j-1} - Z'_{j-2})\right]\right\}$$

$$\times \exp\left\{-\frac{2}{\cos\Theta}\left[\alpha'_j Z'_{j-1} - \alpha_j Z_{j-1} + Z(\alpha_j - \alpha'_j)\right]\right\} \qquad (41)$$

The effects of making specific errors in the atmospheric attenuation model may be easily derived from Equation (41). For example, if the only error in the atmospheric model is in the boundary-layer total attenuation α_{BL}, then the ratio of Equation (41) for $Z > Z_{BL}$ reduces to

$$\frac{\beta'(R_b)}{\beta(R_b)} = \exp\left\{-2(\alpha'_{BL} - \alpha_{BL})\left[R_s - (Z_{BL} - Z_L)/\cos\Theta\right]\right\} \qquad (42)$$

which is independent of Z (i.e., R_b). Note that a prudent choice of R_s and Θ in Equation (42) could eliminate errors in β due to any inaccuracy in

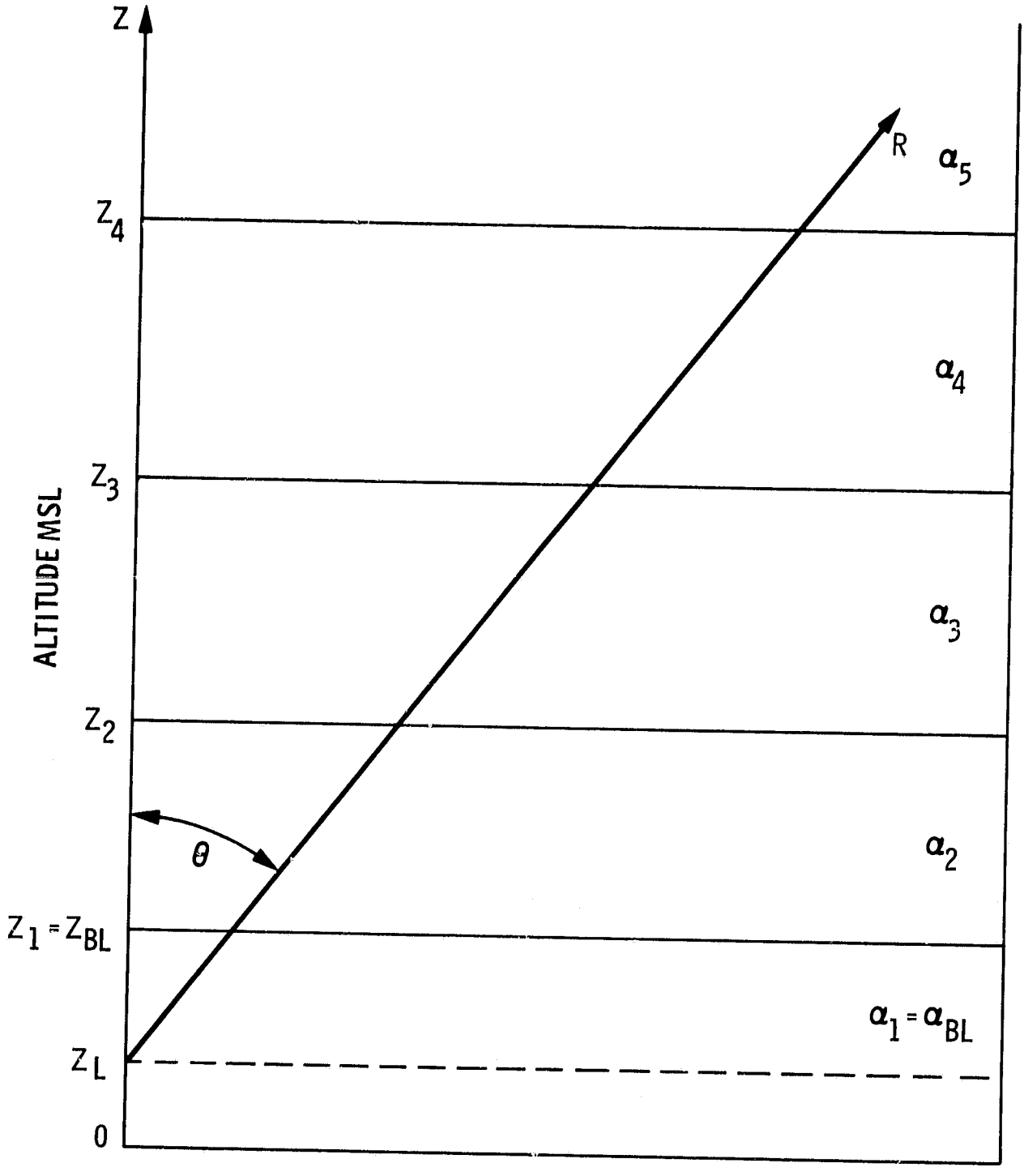

Figure 9. Pictorial representation of the layered atmospheric attenuation model.

α_{BL}. As a second example, consider the only model error to be the height of the boundary layer Z_{BL}. Then Equation (41) becomes

$$\frac{\beta'(R_b)}{\beta(R_b)} = \exp\left\{-\frac{2}{\cos\theta}(Z'_{BL} - Z_{BL})(\alpha_2 - \alpha_{BL})\right\} \tag{43}$$

which is again independent of Z. If the bracketed exponents in Equations (42) and (43) are much smaller than 1, then the percentage error in β will be proportional to the exponents.

We have investigated the altitude dependence of the error in β that results from using various incorrect atmospheric attenuation models. Data from an actual backscatter profile taken on July 21, 1983, at 10.6 μm with $\theta = 0^o$ were used in the investigation, and the results are shown in Figure 10. Our lidar altitude was approximately 0.4 km and the assumed correct atmospheric model was a Midlatitude-Summer model with a 1.5-km boundary-layer altitude and a 0.39 km^{-1} boundary-layer attenuation. Figure 10 gives the percentage error in $\beta(Z)$ resulting from using four "incorrect" atmospheric models: 1) a Midlatitude-Winter model above the boundary layer, 2) a Tropical model above the boundary layer, 3) a Midlatitude-Summer model but with a boundary layer altitude of 1 km, and 4) a Midlatitude-Summer model with a 2-km boundary layer altitude. As predicted by Equation (43), the effects of using an incorrect value of Z_{BL} are independent of altitude. The error due to assuming Z_{BL} = 2 km is ten times the error due to assuming Z_{BL} = 1 km. This is expected from Equation (43), since $(\alpha_2 - \alpha_{BL})$ is much larger for the former case. The use of incorrect atmospheric models above the boundary layer results in an altitude-dependent error in β, as expected from Equation (41). In our example, the error increases with increasing altitude, reaching as much as 30% at 8 km.

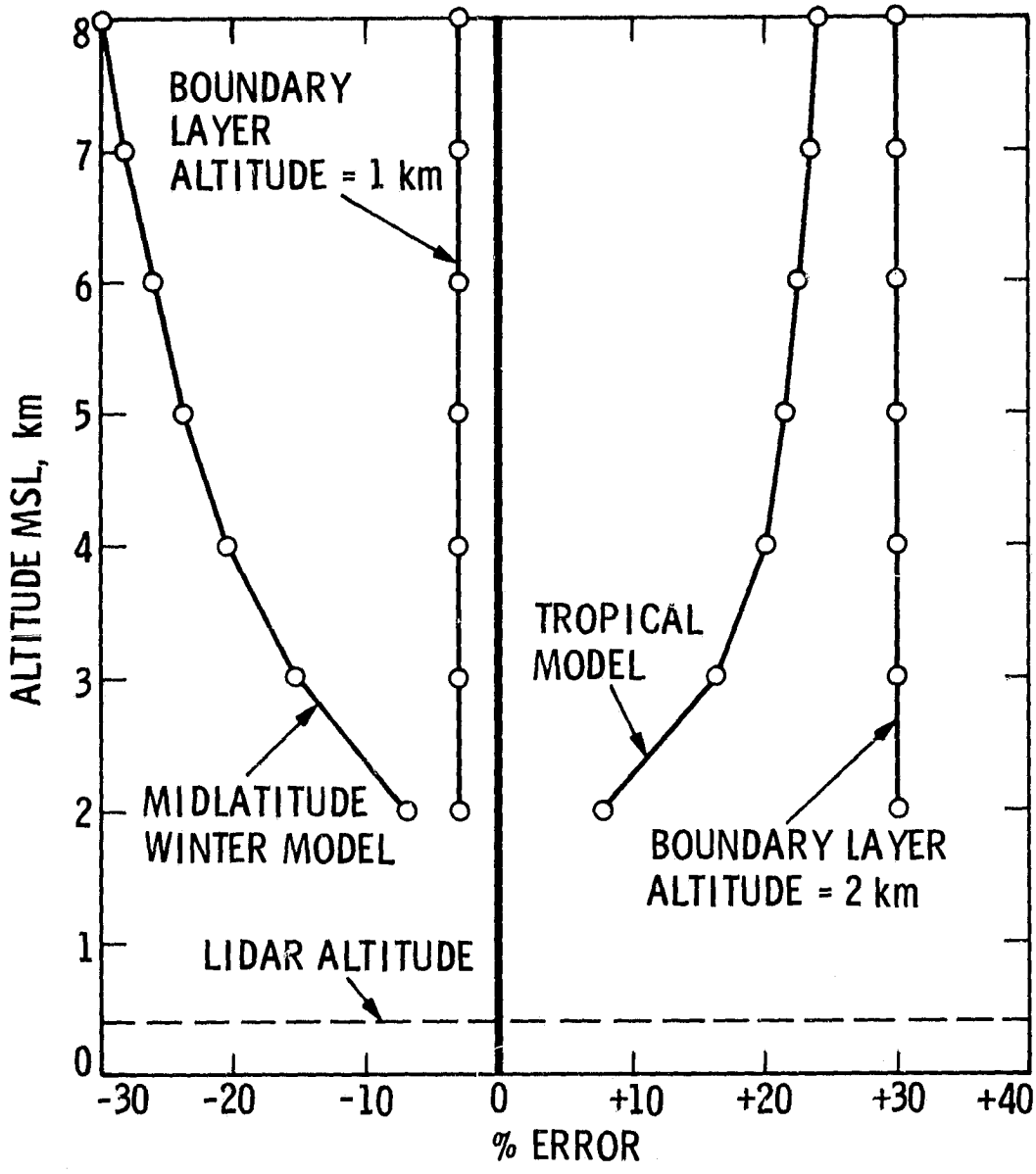

Figure 10. Plot of error vs. altitude in calculated β values resulting from the assumption of incorrect atmospheric models or of boundary-layer altitude. The nominal backscatter profile used actual July 21, 1983, backscatter data at the 10P(20) CO_2 laser line; a Midlatitude-Summer temperature, pressure, and humidity profile; and a boundary-layer altitude of 1.5 km.

It is clear from these results that an incorrect atmospheric attenuation model can easily lead to ±30% errors in the calculated values of β. Correct modeling of the boundary layer is important for upward-pointing lidars that pass through a significant boundary layer. Of course, the boundary-layer effect on downward-pointing lidar data is much less significant.

Other factors that may have to be considered in modeling the atmosphere, depending on the lidar geometry and operating wavelength, include multiple scattering (Tam, 1983), Rayleigh scattering (Sroga et al., 1983) and the effect of the laser pulse on the atmospheric parameters (Fowler, 1983). Multiple scattering and Rayleigh scattering become relatively more important at shorter wavelengths and should be considered when using lidar at, e.g., 1 μm. Fowler (1983) indicates that transmitted pulse fluences of 1 J/cm^2 or greater at CO_2 laser wavelengths may alter the characteristics of fog or aerosols composed largely of water. The pulse fluences of typical coherent lidars used in atmospheric studies are below 0.1 J/cm^2.

SECTION 8

CONCLUSIONS

Several possible sources of systematic error in interpreting and calibrating lidar aerosol backscatter data have been reviewed in this report. In addition to the difficulties posed by the physics of the measurement, other areas of concern that were discussed include data acquisition, data processing, hard-target calibration of the data, and modeling of the telescope overlap function and the atmospheric attenuation. In each case, examples of the resulting error due to incorrect data reduction, data interpretation, calibration, or modeling were given. The largest potential source of error was due to incorrectly modeling (or neglecting) the telescope overlap function. Although the other potential error sources were smaller, they each must be considered in relation to the desired measurement accuracy of the backscatter coefficient.

It is hoped that this discussion will contribute to more accurate and consistent calibration of lidar data through increased understanding of the necessary steps in data interpretation and calibration. Although the viewpoint pertained primarily to stationary, pulsed-CO_2 lidar measurements, much of the analysis should be useful for ground-mobile and airborne lidars, for lidars operating at other wavelengths, and for cw-focused lidars.

It is believed that careful consideration of the calibration-process steps described here will allow significant improvement in the accuracy, calibration, consistency, and inter-calibration between different systems of lidar aerosol backscatter data.

REFERENCES

R. N. Bracewell, The Fourier Transform and Its Applications, McGraw-Hill, New York (1978).

M. C. Fowler, "Effect of a CO_2 laser pulse on transmission through fog at visible and IR wavelengths," Appl. Opt., 22(19), 2960 (1983).

M. J. Kavaya, R. T. Menzies, D. A. Haner, U. P. Oppenheim, and P. H. Flamant, "Target reflectance measurements for calibration of lidar atmospheric backscatter data," Appl. Opt., 22(17), 2619 (1983).

J. D. Klett, "Stable analytical inversion solution for processing lidar returns," Appl. Opt., 20(2), 211 (1981).

J. D. Klett, "Lidar calibration and extinction coefficients," Appl. Opt., 22(4), 514 (1983).

F. X. Kneizys, E. P. Shettle, W. O. Gallery, J. H. Chetwynd, Jr., L. W. Abreu, J. E. A. Selby, R. W. Fenn, and R. A. McClatchey, Atmospheric Transmittance/Radiance: Computer Code LOWTRAN 5, Air Force Geophysics Laboratory, Hanscom Air Force Base, Massachusetts, AFGL-TR-80-0067 (Feb. 1980).

R. A. McClatchey and A. P. D'Agati, Atmospheric Transmission of Laser Radiation: Computer Code LASER, Air Force Geophysics Laboratory, Hanscom Air Force Base, Massachusetts, AFGL-TR-78-0029 (Jan. 1978).

R. A. McClatchey, R. W. Fenn, J. E. A. Selby, F. E. Volz, and J. S. Garing, Optical Properties of the Atmosphere (Third Edition), Air Force Cambridge Research Laboratories, I. G. Hanscom Field, Bedford, Massachusetts, AFCRL-72-0497 (Aug. 1972).

F. E. Nicodemus, J. C. Richmond, J. J. Hsia, I. W. Ginsberg, and T. Limperis, Geometrical Considerations and Nomenclature for Reflectance, NBS Monograph 160 (Oct. 1977).

L. S. Rothman, R. R, Gamache, A. Barbe, A. Goldman, J. R. Gillis, L. R. Brown, R. A. Toth, J.-M. Flaud, and C. Camy-Peyret, "AFGL atmospheric absorption line parameters compilation: 1982 edition," Appl. Opt., 22(15), 2247 (1983).

P. B. Russell, T. J. Swissler, and M. P. McCormick, "Methodology for error analysis and simulation of lidar aerosol measurements," Appl. Opt., 18(22), 3783 (1979).

K. Sassen and G. C. Dodd, "Lidar crossover function and misalignment effects," Appl. Opt., 21(17), 3162 (1982).

J. T. Sroga, E. W. Eloranta, S. T. Shipley, F. L. Roesler, and P. J. Tryon, "High spectral resolution lidar to measure optical scattering properties of atmospheric aerosols. 2: Calibration and data analysis," Appl. Opt., 22(23), 3725 (1983).

W. G. Tam, "Aerosol backscattering of a laser beam," Appl. Opt., 22(19), 2965 (1983).

D. S. Zrnić, "Moments of estimated input power for finite sample averages of radar receiver outputs," IEEE Transactions on Aerospace and Electronic Systems, AES-11(1), 109 (1975).

APPENDIX A

SYMBOLS AND DEFINITIONS

Symbol	Definition	Units
A	Area	m^2
A_i	Illuminated area	m^2
A_r	Area viewed by receiver	m^2
A_s	Hard-target surface area	m^2
c	Speed of light (2.998×10^8)	$m\ s^{-1}$
C	Capacitance	F
E	Irradiance	$W\ m^{-2}$
E	Energy	J
E_0	Average pulse energy	J
E_i	Energy of pulse $i = E_0 + \varepsilon_i$	J
E_{tb}	Energy transmitted into atmosphere	J
E_{ts}	Energy transmitted toward hard target	J
f	Frequency	Hz, s^{-1}
f_r	Bidirectional reflectance-distribution function	sr^{-1}
F	Operator	-
F_b	Aerosol backscatter operator	-
F_r	Lidar receiver operator	-
F_s	Target backscatter operator	-
F_t	Transmitted-pulse operator	-
G	Gain parameter	-
G_b	Aerosol backscatter gain parameter	-

G_s	Target backscatter gain parameter	-
G_t	Transmitted pulse gain parameter	-
H(t)	Heaviside unit step function (0:t<0; 1:t>0)	-
i	Counting index	-
I_s	Time integral of target return power	J
j	Counting index	-
K	Arbitrary signal	-
L	Radiance	$W\ m^{-2}\ sr^{-1}$
M	Gamma density function parameter	-
N	Number of events	-
N_b	Number of aerosol backscatter pulses	-
N_s	Number of hard-target backscatter pulses	-
O(R)	Telescope overlap function	-
p	Polarization parallel to plane of incidence	-
p(x)	Probability density function	x^{-1}
p(y)	Probability density function	y^{-1}
P	Power	W
P_0	Power of rectangular pulse	W
P_b	Aerosol backscatter received power	W
P_s	Target backscatter received power	W
P_t	Transmitted-pulse power	W
P_{tb}	Transmitted-pulse power into atmosphere	W
P_{ts}	Transmitted-pulse power toward hard target	W
R	Resistance	Ω
R	Range	m
R_b	$c[t/2 - \tau_p/4]$	m

R_s	Range to hard target	m
s	Polarization perpendicular to plane of incidence	-
S	Arbitrary signal	-
t	Time	s
V	Voltage	V
V_b	Aerosol backscatter recorded voltage	V
V_s	Target backscatter recorded voltage	V
V_t	Transmitted pulse recorded voltage	V
V_{tb}	Recorded voltage for transmitted pulse into atmosphere	V
V_{ts}	Recorded voltage for transmitted pulse toward hard target	V
X	Random variable	x
Y	$N^{-1}\ \Sigma X$	x
Z	Altitude	m
Z_{BL}	Altitude of top of boundary layer	m
Z_L	Altitude of lidar apparatus	m
α	Extinction coefficient	m^{-1}
$\alpha_b(R)$	Extinction coefficient along atmospheric path	m^{-1}
α_{BL}	Extinction coefficient of boundary layer	m^{-1}
$\alpha_s(R)$	Extinction coefficient along target path	m^{-1}
β	Aerosol volume backscatter coefficient	$m^{-1}\ sr^{-1}$
$\delta(x)$	Impulse symbol	x^{-1}
ε_i	Deviation of ith laser pulse energy from E_0	J
η	Optical efficiency	-
Θ	Polar angle	rad

λ	Optical wavelength	m
π	3.14159	-
$\rho(\omega_i;\omega_r)$	Biconical reflectance	-
ρ_{IS}	Directional-hemispherical reflectance, $\rho(\theta_i,\phi_i;2\pi)$	-
ρ^*	Target reflectance parameter	sr^{-1}
τ	Time constant	s
τ_b	Aerosol backscatter time constant	s
τ_p	Transmitted pulse duration	s
τ_s	Target backscatter time constant	s
τ_t	Transmitted pulse time constant	s
ϕ	Azimuthal angle	rad
Φ	Radiant flux	W
ω	Solid angle	sr
ω_i	Incident irradiance solid angle	sr
ω_r	Receiver solid angle	sr
$\langle x \rangle$	Average value	-

APPENDIX B

BIBLIOGRAPHIES

Flame-sprayed aluminum

"Recommended Practices for Metallizing with Aluminum and Zinc for Protection of Iron and Steel," American Welding Society, Inc., New York, AWS C2.2-67 (1967).

R. A. Brandewie and W. C. Davis, "Parametric study of a 10.6-μ laser radar," Appl. Opt., 11(7), 1526 (1972).

Bidirectional Reflectance: Definitions, Discussion, and Utilization (Vol. I) and Bidirectional Reflectance: Graphic Data (Vol. II), Target Signature Analysis Center, Infrared and Optics Division, Willow Run Laboratories, University of Michigan, Ann Arbor, AFAL-TR-72-226 (Oct. 1972).

"Flame Spraying," Department of the Air Force, Washington, D.C., MIL-STD-869A (Nov. 1972).

R. H. Kohl, "Final Report: The Opposition Effect at 10 Micrometers," The University of Tennessee Space Institute, Tullahoma, Tennessee (Aug. 1980).

M. J. Kavaya, R. T. Menzies, D. A. Haner, U. P. Oppenheim, and P. H. Flamant, "Target reflectance measurements for calibration of lidar atmospheric backscatter data," Appl. Opt., 22(17), 2619 (1983).

Flowers of sulfur

J. T. Agnew and R. B. McQuistan, "Experiments concerning infrared diffuse reflectance standards in the range 0.8 to 20.0 microns," J. Opt. Soc. Am., 43(11), 999 (1953).

C. MacNeill, "Infrared transmittance of rhombic sulfur," J. Opt. Soc. Am., 53(3), 398 (1963).

M. Kronstein, R. J. Kraushaar and R. E. Deacle, "Sulfur as a standard of reflectance in the infrared," J. Opt. Soc. Am., 53(4), 458 (1963).

W. R. Blevin and W. J. Brown, "An infra-red reflectometer with a spheroidal mirror," J. Scient. Instrum., 42, 385 (1965).

W. Wm. Wendlandt and H. G. Hecht, "Reflectance spectroscopy," in Chemical Analysis, A Series of Monographs on Analytical Chemistry and its Applications (Vol. 21), P. J. Elving and I. M. Kolthoff, eds., Interscience Publishers, John Wiley & Sons, New York (1966).

W. G. Egan and T. Hilgeman, "Integrating spheres for measurements between 0.185 μm and 12 μm," Appl. Opt., 14(5), 1137 (1975).

M. J. Post, "Field calibration and discussion of various coherent lidar targets," Digest of the NOAA/OSA Topical Meeting on Coherent Laser Radar for Atmospheric Sensing, Aspen, Colorado (July 15-17, 1980).

M. J. Post, R. A. Richter, R. J. Keeler, R. M. Hardesty, T. R. Lawrence and F. ". Hall, "Calibration of coherent lidar targets," Appl. Opt., 19(16), 2828 (1980).

M. J. Kavaya, R. T. Menzies, D. A. Haner, U. P. Oppenheim, and P. H. Flamant, "Target reflectance measurements for calibration of lidar atmospheric backscatter data," Appl. Opt., 22(17), 2619 (1983).

A. Gross, "Polarization of reflected 10.6 μm radiation from sublimed sulfur targets," Appl. Opt., 22(19), 3031 (1983).

Laser Remote Sensing

E. D. Hinkley, ed., Laser Monitoring of the Atmosphere, Springer-Verlag, Berlin (1976).

D. K. Killinger and A. Mooradian, eds., Optical and Laser Remote Sensing, Springer-Verlag, Berlin (1983).

R. M. Measures, Laser Remote Sensing: Fundamentals and Applications, Wiley-Interscience, John Wiley & Sons, New York (1984).

Reflectance Nomenclature

F. E. Nicodemus, "Directional reflectance and emissivity of an opaque surface," Appl. Opt., 4(7), 767 (1965).

D. B. Judd, "Terms, definitions, and symbols in reflectometry," J. Opt. Soc. Am., 57(4), 445 (1967).

F. E. Nicodemus, "Reflectance nomenclature and directional reflectance and emissivity," Appl. Opt., 9(6), 1474 (1970).

F. E. Nicodemus, ed., Self-Study Manual on Optical Radiation Measurements: Part I -- Concepts, Chapters 1 to 3, NBS Technical Note 910-1 (Mar. 1976).

J. C. Richmond and J. J. Hsia, "Bidirectional reflectometry. Part II. Bibliography on scattering by reflection from surfaces," J. Res. Nat. Bur. Stand.-A. Phys. and Chem., 80A(2), 207 (1976).

F. E. Nicodemus, J. C. Richmond, J. J. Hsia, I. W. Ginsberg, and T. Limperis, Geometrical Considerations and Nomenclature for Reflectance, NBS Monograph 160 (Oct. 1977).

F. E. Nicodemus, "Radiance," Am. J. Phys., 31, 368 (1983).

Telescope Overlap Function

T. Hirschfeld, "Range independence of signal in variable focus remote Raman spectrometry," Appl. Opt., 13(6), 1435 (1974).

T. Halldorsson and J. Langerholc, "Geometrical form factors for the lidar function," Appl. Opt., 17(2), 240 (1978).

J. Harms, W. Lahmann, and C. Weitkamp, "Geometrical compression of lidar return signals," Appl. Opt., 17(7), 1131 (1978).

J. Harms, "Lidar return signals for coaxial and noncoaxial systems with central obstruction," Appl. Opt., 18(10), 1559 (1979).

W. S. Heaps, "Differential absorption lidar errors caused by misalignment in coaxial systems," Digest of the Eleventh International Laser Radar Conference, Madison, Wisconsin, paper C8 (June 1982).

K. Sassen and G. C. Dodd, "Lidar crossover function and misalignment effects," Appl. Opt., 21(17), 3162 (1982).